JGR Planets

RESEARCH ARTICLE
10.1029/2021JE006939

Determining the Effect of Varying Magmatic Volatile Content on Lunar Magma Ascent Dynamics

M. Lo[1], G. La Spina[1,2], K. H. Joy[1], M. Polacci[1], and M. Burton[1]

[1]Department of Earth and Environmental Sciences, University of Manchester, Manchester, UK, [2]Istituto Nazionale di Geofisica e Vulcanologia Sezione di, Catania, Sicilia, Italy

Key Points:

- We use a magma ascent model and sensitivity analysis to understand the relative significance of different volatiles on lunar magma ascent
- For the range of initial volatile abundances considered, CO and H_2 were more significant than H_2O in driving lunar magma ascent
- Results highlight the importance of quantifying and determining the origin of CO, and understanding H-speciation within the lunar mantle

Supporting Information:

Supporting Information may be found in the online version of this article.

Correspondence to:

M. Lo,
marissa.lo@manchester.ac.uk

Citation:

Lo, M., La Spina, G., Joy, K. H., Polacci, M., & Burton, M. (2021). Determining the effect of varying magmatic volatile content on lunar magma ascent dynamics. *Journal of Geophysical Research: Planets*, *126*, e2021JE006939. https://doi.org/10.1029/2021JE006939

Received 5 MAY 2021
Accepted 1 OCT 2021

Author Contributions:

Conceptualization: M. Lo, G. La Spina, K. H. Joy, M. Polacci, M. Burton
Formal analysis: M. Lo, G. La Spina
Investigation: M. Lo, G. La Spina
Methodology: M. Lo, G. La Spina
Supervision: G. La Spina, K. H. Joy, M. Polacci, M. Burton
Visualization: M. Lo
Writing – original draft: M. Lo
Writing – review & editing: M. Lo, G. La Spina, K. H. Joy, M. Polacci, M. Burton

Abstract The Moon is not volcanically active at present, therefore, we rely on data from lunar samples, remote sensing, and numerical modeling to understand past lunar volcanism. The role of different volatile species in propelling lunar magma ascent and eruption remains unclear. We adapt a terrestrial magma ascent model for lunar magma ascent, considering different compositions of picritic magmas and various abundances of H_2, H_2O, and CO (measured and estimated) for these magmas. We also conduct a sensitivity analysis to investigate the relationship between selected input parameters (pre-eruptive pressure, temperature, conduit radius, and volatile content) and given outputs (exit gas volume fraction, velocity, pressure, and mass eruption rate). We find that, for the model simulations containing H_2O and CO, CO was more significant than H_2O in driving lunar magma ascent, for the range of volatile contents considered here. For the simulations containing H_2 and CO, H_2 had a similar or slightly greater control than CO on magma ascent dynamics. Our results showed that initial H_2 and CO content has a strong control on exit velocity and pressure, two factors that strongly influence the formation of an eruption plume, pyroclast ejection, and overall deposit morphology. Our results highlight the importance of (a) quantifying and determining the origin of CO, and (b) understanding the abundance of different H-species present within the lunar mantle. Quantifying the role of volatiles in driving lunar volcanism provides an important link between the interior volatile content of the Moon and the formation of volcanic deposits on the lunar surface.

Plain Language Summary Unlike the Earth, the Moon does not have any active volcanoes, and has not had any active volcanoes for at least the last 100 million to 1 billion years. Therefore, we rely on studying samples collected by astronauts and robotic landers, satellite data, and computer models to understand what volcanic activity on the Moon was like. Volcanic eruptions are mostly driven by gas: as magma rises in the Moon's crust, gases will separate out, allowing magma to rise more quickly. As a result of this, we can use volcanic eruptions to understand how much gas exists within the Moon, which is important for understanding how the Moon formed. We used a computer model to simulate magma ascent on the Moon in order to understand what gases were more significant in driving magma ascent. We found that molecular hydrogen and carbon monoxide had a bigger effect on magma ascent than water, so would have a greater effect on the style of volcanic eruptions on the Moon. The source of carbon monoxide and the relative amounts of molecular hydrogen and water in the Moon's mantle are currently unknown and our results highlight the importance of understanding this information for understanding lunar volcanic activity.

1. Introduction

1.1. Lunar Pyroclastic Deposits

Volcanism is a key process that links the interior of a planetary body to its surface, and therefore understanding lunar volcanic processes can help us understand the volatile content of the lunar interior (Anand et al., 2014; Grove & Krawczynski, 2009; Rutherford et al., 2017). Data from lunar samples, remote sensing, and modeling are key tools in understanding lunar volcanism (Basaltic Volcanism Study Project, 1981; Jolliff et al., 2006).

Lunar pyroclastic glass beads have been a significant source of information for studying volcanic activity on the Moon (Elkins-Tanton et al., 2003a). Pyroclastic material has been found on the surface of the Moon in many of the returned lunar soil samples (Delano, 1986; Heiken et al., 1974) and via remote sensing data (Carter et al., 2009; Gaddis et al., 1985; Hawke et al., 1989). Not only do these pyroclastic glass beads provide

evidence that the Moon experienced explosive volcanism, rather than solely effusive volcanism (Coombs & Hawke, 1992; Morgan et al., 2021; Wilson & Head, 1981), they have also been important samples for researching the volatile content of the Moon's mantle (Hauri et al., 2011; Saal et al., 2008). These pyroclasts are picritic in composition (containing <52 wt % SiO_2 and >12 wt % MgO [Le Bas, 2000]), spherical to ovoid in shape, occasionally host olivine phenocrysts (Hauri et al., 2011), have a glassy or devitrified texture, and are analogous to terrestrial Pele's tears (Moune et al., 2007). Based on the lack of impact metamorphic shock textures and textural and chemical homogeneity, it has been largely accepted that these pyroclastic glass beads were produced by explosive volcanic activity (Carter et al., 2009; Coombs & Hawke, 1992; Weitz et al., 1998). Compositionally, the pyroclastic glasses are grouped by their TiO_2 content, from very low-Ti (<1% TiO_2), to low-/intermediate-Ti (1%–6% TiO_2), to high-Ti (>6% TiO_2), which correspond to the colors green, yellow, and orange/red/black respectively (Neal & Taylor, 1992).

The pyroclastic glass beads have been observed as a component within the regolith at all Apollo landing sites (Delano, 1986; Heiken et al., 1974), but are also found in concentrated deposits. These concentrated deposits of pyroclastic glass beads are termed dark mantling deposits, based on their low albedo in spectral data and interaction with preexisting topography (Gaddis et al., 1985, 2003). Over 100 dark mantling deposits have now been identified across the Moon, with the majority of these located on the lunar nearside (Gustafson et al., 2012). These deposits have been categorized by their areal extent as local (~250–550 km^2) or regional (>1,000 km^2), with a roughly equal number of deposits split between these two categories (Gaddis et al., 2000; Weitz et al., 1998). It has been widely agreed that the volcanic eruptions that produced the picritic glass beads were analogous to lava fountain eruptions (Carter et al., 2009; Coombs & Hawke, 1992; Elkins-Tanton et al., 2003a), with localized and regional dark mantling deposits produced by eruptions equivalent to terrestrial Vulcanian and Strombolian eruption styles respectively (Head & Wilson, 1979).

1.2. Measuring Volatiles in Lunar Pyroclastic Glass Beads

The discovery of measurable amounts of H in lunar pyroclastic glasses and melt inclusions (Hauri et al., 2011; Saal et al., 2008) led to a paradigm shift from viewing the Moon's mantle as dry (Shearer et al., 2006) to relatively wet, likely heterogeneously so (McCubbin et al., 2015). Many studies have followed this discovery, aiming to quantify the abundance of H (as OH and equivalent H_2O) and other volatiles in the lunar mantle (Boyce et al., 2010; Hauri et al., 2011; Tartèse et al., 2013; Wang et al., 2012). The huge body of research dedicated to understanding H_2O and other volatiles in the lunar interior has clear implications for understanding the formation, thermal history, and volcanic history of the Moon (Anand et al., 2014; Hartmann, 2014; Hartmann & Davis, 1974).

While progress has been made in quantifying lunar volatiles from lunar samples, it is still not clear what role different volatile elements had during magma ascent and volcanic eruptions on the Moon. Since the Moon has not been volcanically active for at least 100 Ma (Braden et al., 2014), likely not for the last 1 Ga (Hiesinger et al., 2011), it is difficult to understand past active volcanic processes. To this aim, numerical models of magma ascent provide an invaluable tool to investigate and understand the processes and dynamics that occurred during volcanic eruptions.

1.3. Magma Ascent Modeling

Magma ascent is a complex process since it comprises numerous, interrelated processes that have significant effects, such as crystallization, degassing, temperature, pressure, and rheological changes (La Spina et al., 2015). Individually, each of these processes can already have a significant effect on magma ascent dynamics (Caricchi et al., 2007; Dingwell & Webb, 1989; Sigurdsson, 2015; Webb & Dingwell, 1990). However, they can also affect each other in non-linear ways, producing feedbacks and interactions we cannot readily anticipate by studying them separately. An example of this is the temperature within the conduit, which is affected by both the adiabatic cooling due to bubble expansion and by the heating resulting from the release of latent heat of crystallization (La Spina et al., 2015). The temperature resulting from the balance of these processes then affects the rheology of magma, which, in turn, alters the velocity of ascent. This influences the time available for crystals to grow, and consequently, the release of latent heat, producing a feedback on the temperature itself, which can be only quantified by considering all these processes simultaneously.

Overall, it is extremely important to incorporate all of these processes into a holistic, quantitative, and comprehensive model for magma ascent.

Early models for magma ascent on Earth and on the Moon did not account for the presence of multiple gas phases, crystals, gas-magma separation, or temperature variation (Wilson, 1980; Wilson & Head, 1981). Over time, models began to consider the presence of crystals (Papale & Dobran, 1994), the presence of multiple gas phases (Papale, 1999, 2001), and variations in source temperature (Costa et al., 2007; Melnik & Sparks, 2002), although these additional complexities have mostly been confined to terrestrial magma ascent models rather than lunar magma ascent models. Most models for lunar magma ascent have either been theoretical (Wilson & Head, 2017) or focused more on the rock mechanics aspect of magma ascent (Lister & Kerr, 1991; Wilson & Head, 2003) rather than the magmatic aspect. Numerical models for lunar magma ascent have been explored, such as in Rutherford and Papale (2009), where they modeled the ascent of an intermediate- to high-Ti, orange picrite from 8 km depth to the lunar surface, using a fixed temperature. Through this, they were able to quantify the gas volume fraction during ascent and the exit velocity, as well as predict that magma fragmentation would occur once the magma reached the lunar surface.

To investigate the role of different volatile species (H_2, H_2O, and CO) on lunar magma ascent, we use a numerical model for terrestrial magma ascent (Aravena et al., 2018; Carr et al., 2018; de' Michieli Vitturi et al., 2011; La Spina et al., 2015, 2021), that has been adapted for the Moon. The model we present here incorporates the parameters and processes mentioned above, providing a holistic approach, where the petrological, thermodynamic, rheological, and degassing processes are all addressed, quantified, and combined together.

Overall, in this study we aim to (a) quantify the effect of varying magmatic volatile content on magma ascent dynamics on the Moon, (b) understand the relative importance of different magmatic volatiles on magma ascent dynamics, and (c) compare and contrast our results with existing models for lunar magma ascent.

2. Methods

2.1. Model Background

Here we used a one-dimensional, multiphase, steady-state Fortran 90-based model for the ascent of magma in a cylindrical conduit (Aravena et al., 2018; Carr et al., 2018; de' Michieli Vitturi et al., 2011; La Spina et al., 2015, 2021). The magma ascent model consisted of a system of partial differential equations derived from the work of Romenski et al. (2010), which coupled conservation equations for mass, momentum, and energy of the whole mixture, with balance equations describing the evolution of the internal phases within the mixture (such as the evolution of volume and mass fractions and of the gas/liquid slip velocity). The governing equations of the 1D steady-state magma ascent model adopted here are reported in Supporting Information Text S1.

Providing constitutive equations (such as appropriate rheological, crystallization, and exsolution models), equations of state of each phase, boundary conditions (such as fixed pressure or choked flow condition at the vent of the conduit), and input parameters (such as inlet pressure and temperature, radius of the conduit, volatile content, and crystal content), the magma ascent model calculated several quantities within the entire conduit and at the exit vent (such as pressure, temperature, ascent velocity, gas content, crystal content, and viscosity).

The model is versatile and numerous versions have previously been used to address several volcanological questions, such as the complex variation of temperature within a conduit as a result of decompression and gas expansion (which both induce a cooling of the magmatic mixture) and crystallization (which causes a heating of the magmatic mixture) during the ascent of a basaltic magma (La Spina et al., 2015). The model has also been used to constrain characteristic times of crystallization and exsolution (La Spina et al., 2016), showing that syn-eruptive crystallization during effusive and mild lava fountaining requires about two hours to reach equilibrium. Recently, Arzilli et al. (2019) used this magma ascent model to show that a rapid magma ascent during basaltic explosive eruptions (such as Plinian or sub-Plinian eruptions) produces a large undercooling. By performing fast-cooling synchrotron experiments, they found that this large undercooling can induce rapid syn-eruptive crystallization on the order of minutes, and not hours, as for mild lava fountaining activity, increasing viscosity and leading eventually to explosive magma fragmentation. A different version of the model, which considers lateral degassing, has been used by Carr et al. (2018) to calculate the extrusion and ascent

Table 1
Melt Compositions Used in Model, Based on Geochemical Data From the Apollo 11, 15, and 17 Picritic Glass Beads (Binder, 1976; Delano & Lindsley, 1983; Delano & Livi, 1981; Shearer & Papike, 1993; Shearer et al., 1990)

Oxide/ wt. %	Green (very low-Ti)	Yellow (low- to intermediate-Ti)	Orange (high-Ti)	Red (high-Ti)	Black (high-Ti)
SiO_2	45.6	40.5	39.2	33.8	33.9
TiO_2	0.43	7.0	9.0	16.3	16.1
Al_2O_3	7.5	8.2	7.3	4.8	4.4
FeO	19.2	22.2	22.4	23.9	22.5
MnO	0.26	0.24	0.28	0.33	0.25
MgO	17.9	12.2	12.4	13.2	13.8
CaO	8.3	8.8	8.3	6.8	6.4
Na_2O	0.16	0.4	0.4	0.1	0.8
K_2O	0.01	-	0.05	0.175	0.400
P_2O_5	0.03	-	-	-	-
Total	98.96	99.54	99.33	99.405	98.55
Sources	Average of 17 Apollo 15 samples (Binder, 1976; Shearer & Papike, 1993).	Average of 11 samples from Apollo 17 (Delano & Lindsley, 1983).	Average of 61 samples from Apollo 17 (Delano & Lindsley, 1983).	Average of 4 samples from Apollo 12 (Delano & Livi, 1981; Shearer & Papike, 1993).	Average of 7 samples from Apollo 14 (Shearer et al., 1990).

Note. A dashed line means that the data was not reported.

rate of magma during the 2006 effusive eruption of Merapi, Indonesia. Furthermore, following de' Michieli Vitturi et al. (2010), Aravena et al. (2017, 2018) modified the model to allow conduit radius variations with depth in order to investigate conduit stability during explosive eruptions.

2.2. Test Case Scenarios

We investigated the role of volatiles on magma ascent dynamics on the Moon by considering the main five compositions of lunar picritic magmas (Table 1): green (very low-TiO_2), yellow (low- to intermediate-TiO_2), and orange, red, and black (high-TiO_2).

Geochemical data has indicated that lunar picritic glass beads originate from a magma that underwent very little fractional crystallization, since they are enriched in Mg and Ni, compatible elements that are usually incorporated into common minerals, like olivine (Taylor et al., 1991). As a result, picritic pyroclastic glass beads represent primary partial melting of lunar mantle, representing the most primitive lunar material (Hess, 2000; Shearer & Papike, 1993). Hughes et al. (1988) modeled the best fit source region compositions for Apollo 15 green pyroclastic glasses and produced an estimate of between 4% and 7% partial melting of mafic cumulates. Shearer and Papike (1993) also found that mare basalts and picritic pyroclastic glasses do not lie on the same liquid line of descent or crystallization path of cooling, indicating that they originated from source regions of different depths. The source depth of the picritic glasses has previously been calculated using phase relationships and experimental petrology (Delano, 1980). Brown and Grove (2015) used high-pressure, high-temperature pistons to determine the conditions under which intermediate-TiO_2, yellow picritic glass beads would be in equilibrium with different cumulate minerals. It was concluded that olivine and low-Ca pyroxene cumulates would be in equilibrium with the picritic melts at pressures of 2.4–3.0 GPa, equivalent to lunar mantle depths of 512–646 km. Furthermore, by analyzing the volatile phases present in Apollo 15 green glass beads, Elkins-Tanton et al. (2003b) proposed that the glasses originated from pressures of roughly 2.2 GPa, corresponding to roughly 450 km depth.

2.3. Constitutive Equations

The constitutive equations of the magma ascent model relate the governing equations to a specific magmatic system, in this case, the ascent of picritic magmas within the lunar crust (see Text S1 in Supporting Infor-

mation S1). With respect to constitutive equations previously used by La Spina et al. (2015, 2016, 2017, 2019, 2021) to simulate magma ascent at Stromboli, Etna, Kilauea, and Sunset Crater volcanoes, we modified the rheological model to consider the composition of the lunar picritic magmas described in Section 2.2. We also considered different volatile components (see Section 2.3.2) and the corresponding solubility models. The new constitutive equations adopted in this work are described in the sections below (see Table S1 in Supporting Information S1 for symbols used in equations).

The friction with the wall of the conduit was modeled as a function of the Reynolds number, as detailed in La Spina et al. (2019). Laminar and turbulent flows were considered with the corresponding friction factors according to the flow regime (Colebrook, 1939; Fang et al., 2011, La Spina et al., 2019). We assumed a constant crystal content of 1 vol.% in agreement with calculations completed using MELTS (Ghiorso & Gualda, 2015; Gualda et al., 2012): see Text S2 and Datasets S1–S2 in Supporting Information S1. For fragmentation, we utilized the strain rate model by Papale (1999), which suggests that fragmentation would occur when the Deborah number, the ratio between the Maxwell relaxation time and the timescale of deformation (Webb & Dingwell, 1990), exceeds the critical value of 0.01. For outgassing, we adopted a permeable gas flow regime using the Forchheimer's law to describe outgassing below the fragmentation depth (Degruyter et al., 2012; La Spina et al., 2017), while the drag model for gas-ash flow illustrated by Yoshida and Koyaguchi (1999) was used above the fragmentation depth. Finally, the gravitational acceleration was changed from 9.81 to 1.62 m s^{-2}, reflecting the gravitational force on the Moon.

2.3.1. Rheology

The viscosity was calculated using the Costa (2005) model:

$$\mu_l = \mu_{\text{melt}} \cdot \theta_c \cdot \theta_b, \tag{1}$$

where μ_l is the viscosity of the magma, μ_{melt} is the viscosity of the bubble-free, crystal-free liquid phase, θ_c is a factor that increases viscosity due to the presence of crystals, and θ_b is a factor that takes into account the effect of bubbles on the magmatic mixture. To estimate μ_{melt} we adopted the viscosity model of Giordano et al. (2008), using the melt compositions for lunar magmas reported in Table 1.

The presence of crystals was accounted for by θ_c as described in Costa et al. (2009):

$$\theta_c = \frac{1+\varphi^{\delta}}{\left[1-F\left(\varphi,\xi,\gamma\right)\right]^{B\phi^*}}, \tag{2}$$

where

$$F = \left(1-\xi\right) erf\left[\frac{\sqrt{\pi}}{2\left(1-\xi\right)}\varphi\left(1+\varphi^{\gamma}\right)\right], \quad \varphi = \frac{\left(\sum_{j=1}^{n_c} x_{c_j}^{l}\right)}{\phi^*}. \tag{3}$$

The fitting parameters B,δ,ξ,γ, and ϕ^* chosen for this work are the same used in Giordano and Dingwell (2003): $B = 2.8$, $\delta = 13-\gamma$, $\xi = 0.0327$, $\gamma = 0.84$.

The relative viscosity due to the presence of bubbles was calculated using the general formula by Llewellin et al. (2002) and Mader et al. (2013):

$$\theta_b = \theta_{b,\infty} + \frac{\theta_{b,0}-\theta_{b,\infty}}{1+\left(K\,Ca\right)^m} \tag{4}$$

$$\theta_{b,0} = \left(1-\alpha_g\right)^{-1} \tag{5}$$

$$\theta_{b,\infty} = \left(1-\alpha_g\right)^{\frac{5}{3}} \tag{6}$$

where $K = 6/5$ and $m = 2$.

2.3.2. Volatile Solubility

The magma ascent model is able to account for two volatile species; we consider the combinations of H_2O and CO and H_2 and CO throughout this study. Renggli et al. (2017) calculated the relative abundance of various H, O, C, Cl, S, and F-based species in picritic magmas to determine the overall composition of the volcanic gas emitted during an explosive lunar eruption. The study highlighted that the redox conditions present within the lunar mantle are a key control on the type of H-speciation, controlled by the depletion of different volatiles and metals during the formation of the Moon. We know that the lunar mantle has very reducing conditions, with estimates of the oxygen fugacity ranging from +0.2 to −2.5 log units from the iron-wüstite buffer (Fogel & Rutherford, 1995; Shearer & Papike, 2004; Nicholis & Rutherford, 2009). Renggli et al. (2017) concluded that the most abundant gases would be, in descending order of abundance, CO, H_2, H_2S, COS, and S_2, while H_2O was one of the more minor H-species, a result that is consistent with other authors (Sharp et al., 2011).

Using measurements of carbon in lunar volcanic glasses and melt inclusions from Apollo 15 and 17 samples, Wetzel et al. (2015) demonstrated that carbon is present as a dissolved species in lunar magmas. A large number of authors have previously identified CO as a key volatile for driving lunar volcanism and have attributed the production of CO in the lunar mantle to the oxidation of graphite (Fogel & Rutherford, 1995; Nicholis & Rutherford, 2009; Rutherford & Papale, 2009; Sato, 1979; Spudis, 2015; Wetzel et al., 2015; Wilson & Head, 2017). However, graphite has not been detected within any lunar samples as an igneous phase (McCubbin et al., 2015); the only recorded occurrence of graphite has been within an Apollo 17 breccia associated with impact melting (Steele et al., 2010). Fogel and Rutherford (1995) proposed that CO was produced by reactions between C and Fe-, Cr-, and Ti-oxides in the melt; reactions such as this could produce up to 1,000 ppm of CO in low-Ti and intermediate-Ti picrites. The direct dissolution of CO into magma as iron carbonyl ($Fe(CO)_5$) (Wetzel et al., 2013) has also been proposed. Overall, the origin of CO within the lunar mantle remains inconclusive. Organic sources of carbon have also been investigated, following the discovery of complex organic matter on the surface of high-Ti, black pyroclastic glass beads (Thomas-Keprta et al., 2014). It was concluded that the source of the organic carbon is exogenous meteoritic kerogen, delivered to the lunar regolith through micrometeorite impacts, therefore, it is unlikely that this organic carbon would have played a role in magma ascent dynamics.

Although traces of H_2 have not been detected in the volatile-rich coatings of pyroclastic glass beads, we consider H_2 in our magma ascent model as it is more likely to have been present at depth in the mantle based on redox conditions within the lunar mantle (Renggli et al., 2017; Sharp et al., 2011). We also consider H_2O due to the greater amount of information available on the behavior of H_2O at high pressure and temperature, that is, within the Earth's mantle. Several papers present solubility models for H_2O under different conditions (Moore et al., 1995, 1998; Mysen & Wheeler, 2000), whereas H_2 solubility models are less prevalent (Hirschmann et al., 2012). Using H_2O in our lunar magma ascent model is also useful from a comparative planetology perspective, since H_2O is the dominant H-species within terrestrial systems (Holloway & Blank, 1994).

Following La Spina et al. (2015), the mass fraction x_i^{melt} of the dissolved volatile component i (i.e., H_2, H_2O, or CO) was calculated in the conduit model using the nonlinear solubility model:

$$x_i^{\text{melt}} = \sigma_i \left(\frac{P_i}{\overline{P}} \right)^{\epsilon_i}, \tag{7}$$

where P_i is the partial pressure, σ_i is a solubility coefficient, ϵ_i is a solubility exponent, and $\overline{P} = 1$ Pa, a constant value used to make the quantity in brackets adimensional.

To estimate both solubility exponents and coefficients for H_2O, we adopted the model of Moore et al. (1998):

$$2 \ln X_{H_2O}^{\text{melt}} = \frac{a}{T} + \sum_i b_i x_i \left(\frac{P}{T} \right) + c \ln f_{\text{H}_2\text{O}}^{\text{fluid}} + d \tag{8}$$

where $X_{\text{H}_2\text{O}}^{\text{melt}}$ is the mole fraction of H_2O dissolved in the melt, $f_{\text{H}_2\text{O}}^{\text{fluid}}$ is the fugacity of H_2O in the fluid, T is the temperature (Kelvin), P is the pressure (bars), and a is the anhydrous mole fraction of metal oxide com-

ponents. The values of the model coefficients were identical to those used by Moore et al. (1998), $a = 2565$, $b_{Al2O3} = -1.997$, $b_{FeOt} = -0.9275$, $b_{Na2O} = 2.736$, $c = 1.171$, and $d = -14.21$. Best fit values for water solubility exponents and coefficients were calculated for a pressure of 41 MPa and a temperature of 1700 K. For a very low-Ti picrite, a solubility coefficient of 6.15×10^{-7} and exponent of 0.58914 was obtained, while for a high-Ti/black picrite, a solubility coefficient of 5.69×10^{-7} and exponent of 0.59080 was obtained. For all calculated solubility coefficients and exponents, see Table S2 in Supporting Information S1.

For H_2, solubility parameters $\sigma_{CO} = 3.15 \times 10^{-12}$ and $\epsilon_{CO} = 1$ were utilized, based on the solubility curves produced by Hirschmann et al. (2012), assuming a lunar mantle oxygen fugacity of IW −1.0. For CO, solubility parameters $\sigma_{CO} = 0.2438 \times 10^{-12}$ and $\epsilon_{CO} = 1$ were determined using the model by Wetzel et al. (2013), assuming highly reducing conditions in the lunar mantle (Shearer et al., 2006).

2.4. Equations of State

The equations of state describe the internal properties of each phase. For both melt and crystal phases, a linearized version of the Mie-Grüneisen equations of state was adopted (La Spina & de' Michieli Vitturi, 2012; La Spina et al., 2014):

$$\begin{cases} e_k\left(\rho_k, T\right) = \overline{e}_k + c_{v,k}T + \dfrac{\rho_{0,k}C_{0,k}^2 - \gamma_k P_{0,k}}{\gamma_k \rho_k}, \\ P_k\left(\rho_k, T\right) = c_{v,k}\left(\gamma_k - 1\right)\rho_k T - \dfrac{\rho_{0,k}C_{0,k}^2 - \gamma_k P_{0,k}}{\gamma_k}, \\ s_k\left(\rho_k, T\right) = s_{0,k} + c_{v,k}\ln\left[\dfrac{T}{T_{0,k}}\left(\dfrac{\rho_{0,k}}{\rho_k}\right)^{\gamma_k - 1}\right], \\ C_k\left(\rho_k, T\right) = C_{0,k}\sqrt{\left(\dfrac{\rho_k}{\rho_{0,k}}\right)^{\gamma_k - 1}\exp\left(\dfrac{s_k\left(\rho_k, T\right) - s_{0,k}}{c_{v,k}}\right)}, \end{cases} \tag{9}$$

where k indicates either the melt or crystal phase. Here $\overline{e}_k$ is a constant parameter representing the formation energy of the fluid, $c_{v,k}$ is the specific heat capacity at constant volume, γ_k is the adiabatic exponent, $\rho_{0,k}$, $P_{0,k}$, $T_{0,k}$, $s_{0,k}$, and $C_{0,k}$ are respectively the density, pressure, temperature, specific entropy, and speed of sound at a reference state.

For the exsolved gas phase, the Van der Waals equations of state were adopted to take into account the non-ideality of the gas phases (La Spina et al., 2015):

$$\begin{cases} e_{g_i}\left(\rho_{g_i}, T\right) = c_{v,g_i}T - a_{g_i}\rho_{g_i} + \overline{e}_{g_i}, \\ P_{g_i}\left(\rho_{g_i}, T\right) = c_{v,g_i}\left(\gamma_{g_i} - 1\right)T\dfrac{\rho_{g_i}}{1 - b_{g_i}\rho_{g_i}} - a_{g_i}\rho_{g_i}^2, \\ s_{g_i}\left(\rho_{g_i}, T\right) = c_{v,g_i}\log\left[\dfrac{T}{T_{0,g_i}}\left(\dfrac{\rho_{0,g_i}}{\rho_{g_i}}\cdot\left(1 - b_{g_i}\rho_{g_i}\right)\right)^{\left(\gamma_{g_i} - 1\right)}\right], \\ C_{g_i}\left(\rho_{g_i}, T\right) = \sqrt{\dfrac{c_{v,g_i}\left(\gamma_{g_i} - 1\right)\gamma_{g_i}T}{\left(1 - b_{g_i}\rho_{g_i}\right)^2} - 2a_{g_i}\rho_{g_i}} \end{cases} \tag{10}$$

for $i = 1,\ldots,n_g$. The coefficients a_{g_i} and b_{g_i} are defined as

$$a_{g_i} = \frac{27}{64}\frac{c_{v,g_i}^2\left(\gamma_{g_i} - 1\right)^2 T_{c,g_i}^2}{P_{c,g_i}}, \tag{11}$$

$$b_{g_i} = \frac{1}{8}\frac{c_{v,g_i}\left(\gamma_{g_i} - 1\right)T_{c,g_i}}{P_{c,g_i}}, \tag{12}$$

where P_{c,g_i} and T_{c,g_i} are the critical pressure and temperature of the gas component g_i, respectively.

2.5. Initial and Boundary Conditions

The initial conditions for our numerical simulations are defined as a set of values for certain parameters at the inlet of the conduit, which were altered between different model runs. The boundary conditions, instead, are the conditions set at the vent of the conduit. For a given combination of initial and boundary conditions, the model calculated all the parameters within the conduit that satisfied those conditions. Specifically, model solutions were obtained using a shooting technique, which consisted of searching for the inlet magma ascent velocity that allowed us to obtain the desired atmospheric pressure or choked flow condition at the conduit outlet (de' Michieli Vitturi et al., 2008). A choked flow condition is reached when the mixture velocity is equal to the speed of sound in the mixture. To calculate the speed of sound of the mixture, we adopted the equation described in La Spina et al. (2021):

$$C = \frac{1}{\sqrt{K\rho}}, \tag{13}$$

where C is the speed of sound in the mixture, $K = \alpha_l K_l + \alpha_g K_g$ is the compressibility of the mixture, and ρ is the density of the mixture.

For our investigation on how the magmatic volatile content affects magma ascent dynamics on the Moon, we used the five picritic compositions presented in Table 1. For each model run with these compositions, we assumed a conduit radius of 10 m and a conduit depth of 10 km. Compared with larger-scale gravitational anomalies, lunar dykes are difficult to detect and measure using gravimetric data (Andrews-Hanna et al., 2013). We assumed a conduit radius of 10 m to reflect data from surveys of terrestrial dykes that fed basaltic volcanic systems (Anderson, 1951; Kavanagh & Sparks, 2011; Klausen, 2006). Although picrites are thought to originate from depths of up to 450 km (Elkins-Tanton et al., 2003b) or ~600 km depth (Brown & Grove, 2015), we only focus on the final 10 km of ascent, where the role of volatile elements in driving magma ascent is more significant and the direct link to eruption conditions is more feasible.

We considered the pressure, temperature, H_2, H_2O, and CO content, and crystal content as initial conditions at the inlet of the conduit. Values adopted for the model runs are reported in Table 2. Specifically, we set an initial pressure of 41.31 MPa, an initial temperature of 1700 K, and an initial crystal content of 1 vol % (see Text S2 and Datasets S1–S2 in Supporting Information S1) for all model simulations. Regarding the boundary conditions at the conduit outlet, we adopted both a desired pressure at the vent of the conduit and choked flow condition. However, since there is no atmosphere on the Moon, the pressure at the conduit outlet was set to 0 Pa. For the volatile contents, we assumed initial H_2O contents between 25 and 1,500 ppm, based on reported measurements of lunar glass beads (Hauri et al., 2011; Saal et al., 2008), and equivalent H_2 contents between 2 and 85 ppm, based on molecular weight relative to H_2O. Finally, for CO, we assumed the same initial contents as for H_2O, which matches measurements made by Wetzel et al. (2015) at the lower bound and estimates of the carbon content of the terrestrial mantle at the upper bound (Gerlach et al., 2002), Table 2.

2.6. Sensitivity Analysis

We conducted a sensitivity analysis to determine the relationship between various input parameters (inlet temperature and pressure, H_2 content, H_2O content, CO content, and conduit radius) and model outputs for quantities within the conduit (gas volume fraction, exit pressure, exit velocity, and mass flow rate). The sensitivity analysis was performed using the Dakota toolkit (Adams et al., 2014), which is an open-source

Table 2
Initial Conditions at Conduit Inlet Used for Magma Ascent Model Runs in This Study, From Values Reported in the Literature

Initial condition	Value	Assumptions/Reference
Pressure (Pa)	41310000	Based on a conduit depth of 10 km, an acceleration due to lunar gravity of 1.62 m s^{-2}, and average lunar crustal density of 2,550 kg m^{-3} Wieczorek et al. (2013).
Temperature (K)	1700	Liquidus temperatures of 1673 ± 20 K (green and yellow picritic beads) Fogel and Rutherford (1995)) and 1623 K (orange picritic beads) Rutherford and Papale, (2009) have been determined. These values provide a lower bound for this boundary condition.
H_2O content (ppm)	(a) 25 (b) 100 (c) 500 (d) 1,000 (e) 1,500	Initial H_2O content was varied from 25 ppm, based on measurements ranging from 4 to 46 ppm by Saal et al. (2008), and 1,500 ppm, based on measurements of 1,410 ppm by Hauri et al. (2011).
H_2 content (ppm)	(a) 2 (b) 6 (c) 28 (d) 56 (e) 85	Equivalent H_2 content obtained from the conversion of H_2O to molecular hydrogen concentrations.
CO content (ppm)	(a) 25 (b) 100 (c) 500 (d) 1,000 (e) 1,500	The lower limit was based on measurements made by Wetzel et al. (2015), while the upper limit was based on carbon abundances in terrestrial volcanic rocks measured by Hekinian et al. (2000) and Gerlach et al. (2002). The range of initial CO contents were extended to match that of H_2O.
Crystal content (vol %)	1	Initial crystal content of the picritic magma was calculated using MELTS Ghiorso and Gualda (2015); Gualda et al. (2012) and did not exceed 1 weight % for any composition of picrite, assuming an initial liquidus temperature for lunar picritic magma of at least 1693 K Fogel and Rutherford (1995). See Text S1 in Supporting Information S1.

Note. For the initial crystal content calculations, see Text S2 and Datasets S1–S2 in Supporting Information S1.

software produced by Sandia National Laboratories. The software has a broad range of uses including model calibration, risk analyses, and uncertainty quantification. For our sensitivity analyses, we adopted a Latin hypercube sampling technique to vary the different input parameters within set ranges, in a more efficient manner than random sampling (Iman & Conover, 1980; McKay et al., 1979). We performed a sensitivity analysis with H_2O and CO using 10,000 different model simulations for each of the five magma compositions (Table 1), varying the combination of input parameters with a uniform distribution within the ranges considered. An additional sensitivity analysis using H_2 and CO as volatile species for an intermediate-Ti picrite was also performed to compare the results with the corresponding H_2O-CO case. Specifically, the initial temperature was varied between 1600 and 1800 K, the inlet pressure between 40 and 45 MPa, the H_2O and CO content between 5 and 1,500 ppm, the H_2 content between 2 and 90 ppm, and the conduit radius between 10 and 100 m, see Table S3 in Supporting Information S1 for full information.

We chose to analyze four model outputs: gas volume fraction, exit pressure, exit velocity, and mass flow rate. These model outputs have a direct control on many aspects of eruptive behavior, such as the ejection distance of pyroclastic material, the height of an eruption plume, and the overall style of the volcanic eruption (Sigurdsson, 2015; Wilson, 1972; Wilson, 1980).

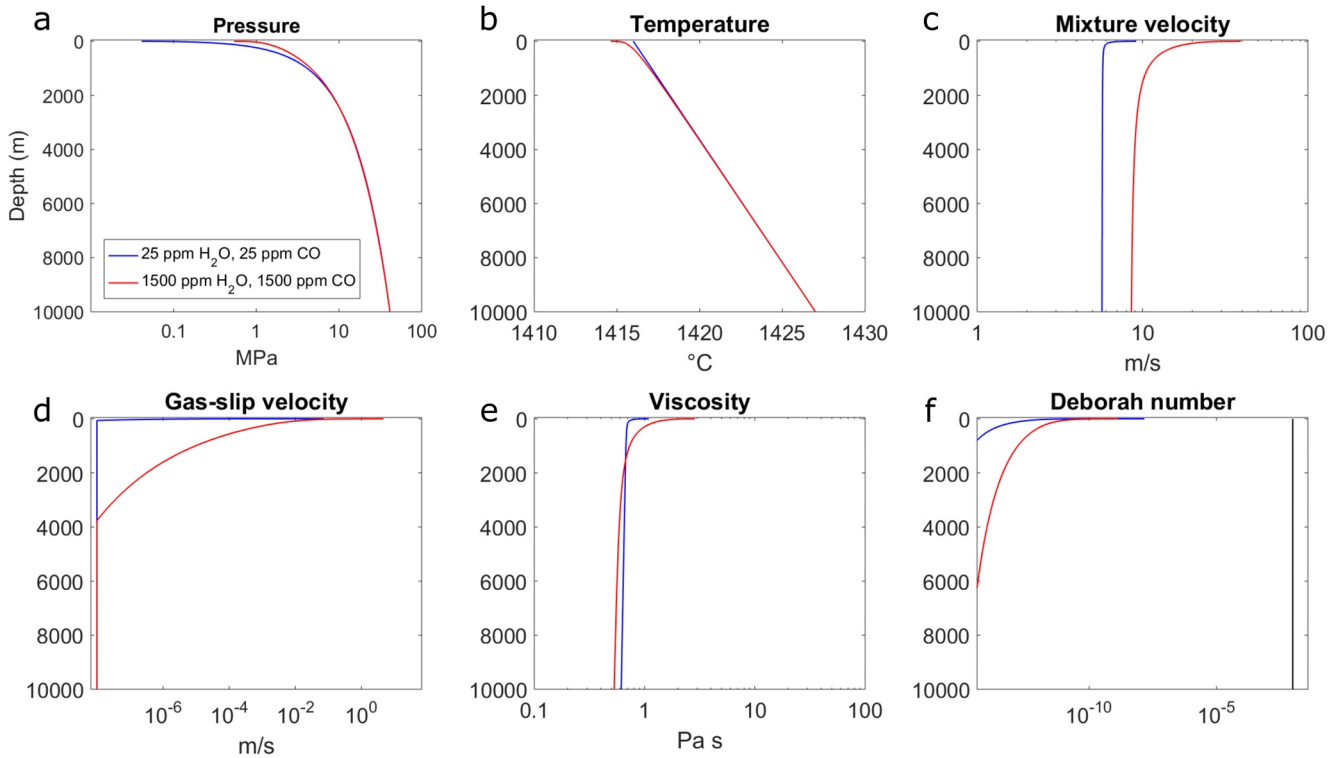

Figure 1. Numerical results for a green/very low-TiO_2 (VLT) picrite with an initial volatile content of 25 ppm H_2O and 25 ppm CO (blue curve) and 1,500 ppm H_2O and 1,500 ppm CO (red curve): (a) pressure, (b) temperature, (c) mixture velocity, (d) gas/melt relative velocity, (e) mixture viscosity, and (f) Deborah number. The black line in panel (f) represents the critical Deborah number above which fragmentation is triggered.

3. Results

3.1. Model Outputs

We present numerical results for (a) the H_2O and CO model simulations and (b) the H_2 and CO model simulations. For the H_2O and CO model simulations, we present results for the two end-member compositions of picrite: green/very low-TiO_2 (VLT) glass (Figure 1), and black/high-TiO_2 glass (Figure 2). In both Figures 1 and 2, we plot the numerical results obtained with a lower volatile content (i.e., 25 ppm of H_2O and 25 ppm of CO, blue lines) and with a higher volatile content (i.e., 1,500 ppm of H_2O and 1,500 ppm of CO, red lines). For the H_2 and CO model simulations, we present results for a green/VLT picrite with a lower bound volatile content of 2 ppm H_2 and 25 ppm CO and an upper bound volatile content of 84 ppm H_2 and 1,500 ppm CO (Figure 3). There was little variation in the results between the five end-member compositions of picrite, for both the H_2O and CO and the H_2 and CO model simulations, therefore, we have chosen to present results from only one or two compositions. For model results for all five magma compositions, see Figures S1–S15 in Supporting Information S1.

The model results presented for H_2O and CO simulations in Figures 1a, 1b, 2a, 2b, 3a, and 3b show a continuous decrease in pressure and temperature for the majority of the conduit. For the lower initial volatile content simulation, an exit pressure of 0.05 MPa was reached, while an exit pressure of 0.6 MPa was reached for the higher initial volatile content simulation. Calculated exit pressure was always greater than zero (the surface pressure on the Moon) so for all simulations the model reached the choked-flow condition at the vent of the conduit.

For the temperature (Figures 1b, 2b, and 3b), we saw a constant cooling of 10°C–15°C after 10 km of ascent. The temperature gradient from the conduit inlet to the surface was relatively low compared to terrestrial low viscosity basaltic magmas (La Spina et al., 2015, 2017, 2021) for two main reasons. First of all, the crystal content was fixed at 1 vol %, therefore, there was no latent heat of crystallization being released into the system (Blundy et al., 2006; La Spina et al., 2015). Second, the volatile content in most of the model simulations

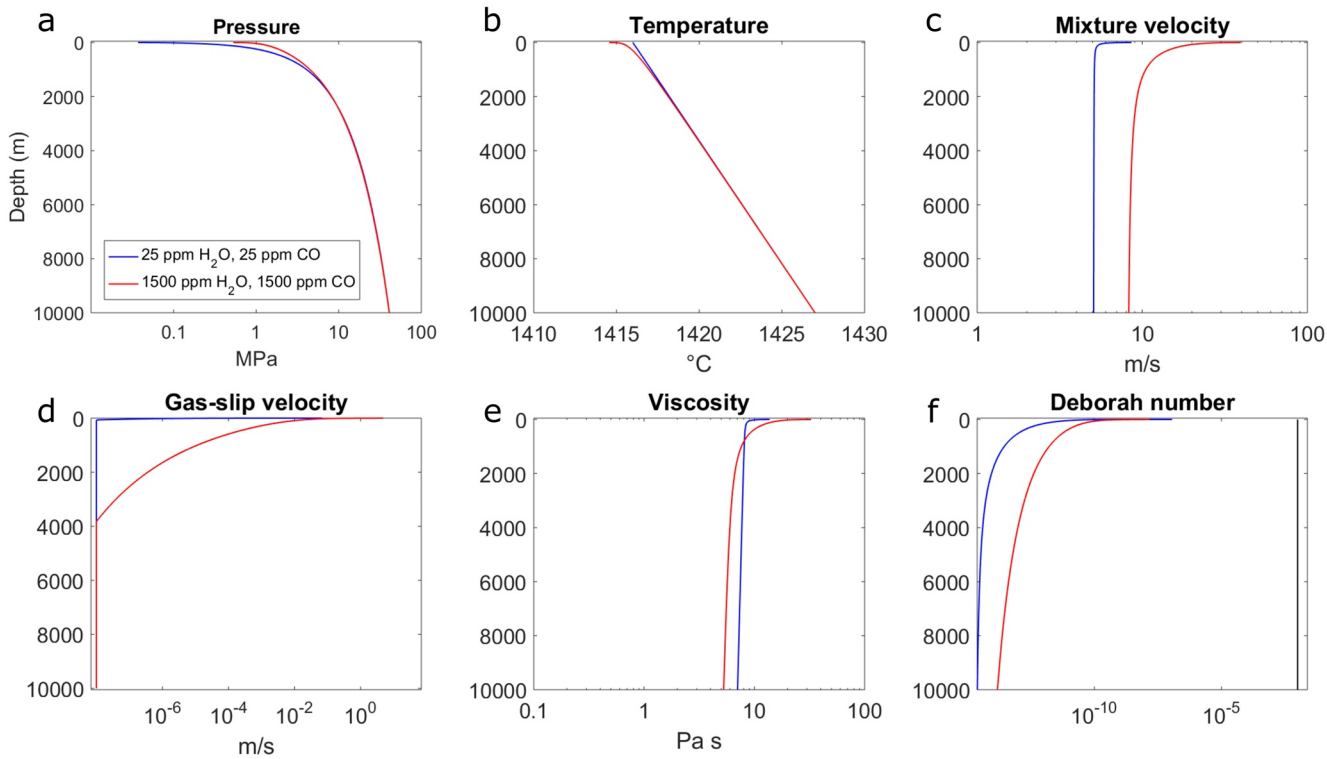

Figure 2. Numerical results for a black/high-Ti picrite with an initial volatile content of 25 ppm H_2O and 25 ppm CO (blue curve) and 1,500 ppm H_2O and 1,500 ppm CO (red curve): (a) pressure, (b) temperature, (c) mixture velocity, (d) gas/melt relative velocity, (e) mixture viscosity, and (f) Deborah number. The black line in panel (f) represents the critical Deborah number above which fragmentation is triggered.

was very low (<0.15 wt.% in total), meaning that there would be little expansion of bubbles during ascent, which limits adiabatic cooling (Kavanagh & Sparks, 2011; La Spina et al., 2015).

For the H_2O and CO model simulations, mixture velocity, gas-melt slip velocity, and viscosity were constant for the majority of the conduit, with changes only occurring within the final 2 km or less of ascent (Figures 1c–1e and 2c–2e). During ascent, mixture velocity was almost constant. From a depth of 10–1 km, a mixture velocity of ~6 m s^{-1} was calculated for the low volatile content simulations, and a mixture velocity of ~8 m s^{-1} was calculated for the high volatile content simulations. From 1 km to the surface, the magma accelerated, with the mixture velocity reaching values of ~10 m s^{-1} (simulations with lower initial volatile contents) to 40 m s^{-1} (simulations with higher initial volatile content). Mixture velocity did not vary significantly across the different compositions. The near constant mixture velocity reflects the low volatile content assumed for the simulated magmas. Indeed, even the higher volatile content simulations do not contain sufficient exsolved volatiles to affect magma buoyancy for most of the conduit, and therefore ascent at depth would be mainly driven by the pressure gradient. It should be noted that these results only represent processes occurring within the conduit, so the ejection velocities are likely to be greater than those reported here, due to the further expansion and acceleration that the magma would experience upon exiting the vent. Gas-melt slip velocity was basically zero from the conduit inlet to the surface for the low volatile content simulations, which means that the bubbles would stay coupled with the melt during ascent, that is, outgassing would be mostly inhibited. For the high volatile content simulations, it appears that bubbles started to decouple from the melt at a depth of ~4 km, however, this does not appear to have affected the overall magma ascent dynamics significantly (Figures 1d and 2d). For the H_2 and CO model simulations, the bubbles appear to begin to decouple from the melt at a greater depth of ~6 km (Figure 3d).

The calculated viscosity of the magma was very low compared to terrestrial simulations for all model simulations, with values of ~0.5–5 Pa s for the very low-TiO_2/green picritic magma, and ~10–30 Pa s for the high-TiO_2/black picritic magma. This is likely a result of the low silica content of picrites, high source tem-

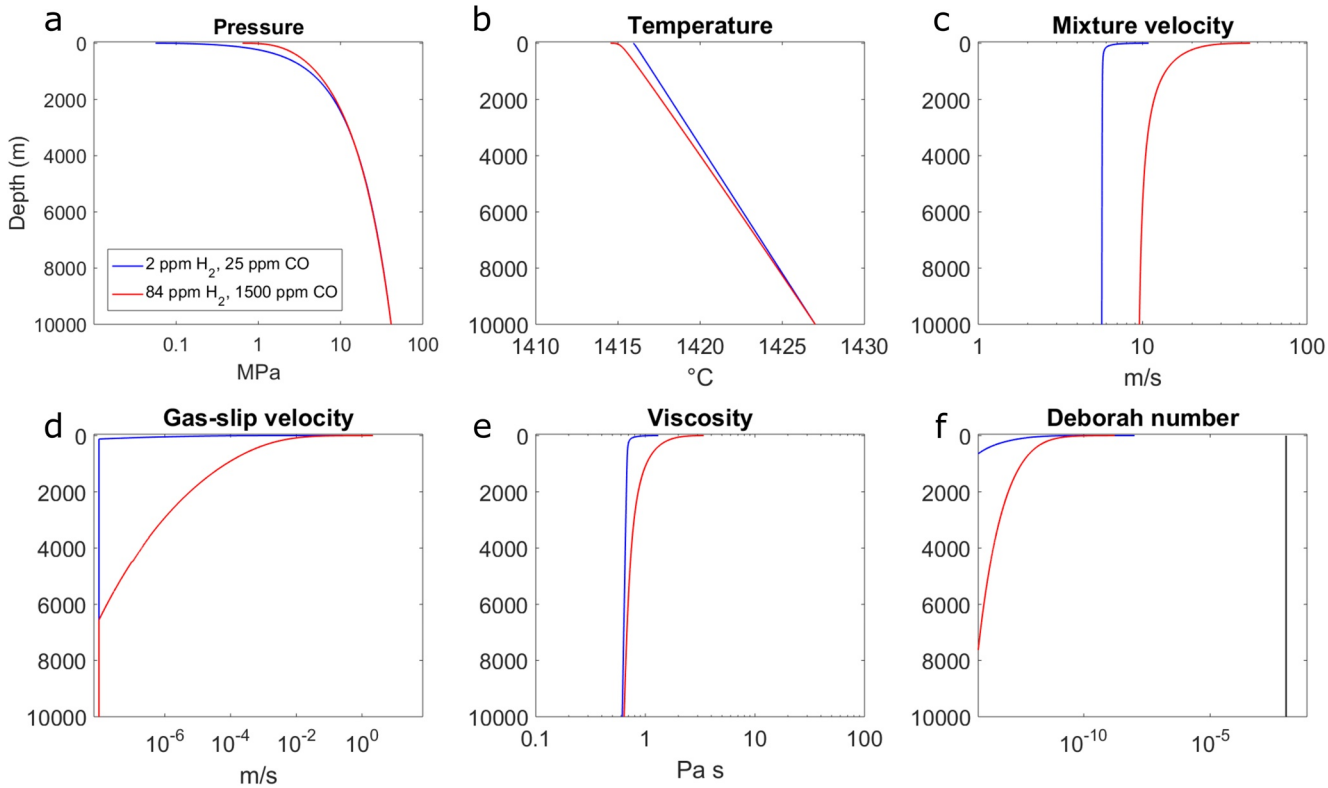

Figure 3. Numerical results for a green/very low-TiO_2 (VLT) picrite with an initial volatile content of 2 ppm H_2 and 25 ppm CO (blue curve) and 84 ppm H_2 and 1,500 ppm CO (red curve): (a) pressure, (b) temperature, (c) mixture velocity, (d) gas/melt relative velocity, (e) mixture viscosity, and (f) Deborah number. The black line in panel (f) represents the critical Deborah number above which fragmentation is triggered.

perature and very low crystal content, which reduces the viscosity of the melt. This result is consistent with viscosity values reported by Williams et al. (2000).

We can see that fragmentation was not expected to occur within the conduit as the critical Deborah number (black lines on Figures 1f, 2f, and 3f) needed to trigger fragmentation (Papale, 1999) was not exceeded. However, the rapid decompression and expansion expected once magma is ejected from the vent due to the negligible pressure outside the conduit would likely trigger inertial or fluid-dynamic fragmentation (Jones et al., 2019, La Spina et al., 2021; Namiki & Manga, 2008). This suggests that the magma would fragment upon reaching the surface, producing a lava fountaining style (La Spina et al., 2021), which is consistent with many models presented previously (Carter et al., 2009; Coombs & Hawke, 1992; Elkins-Tanton et al., 2003a; Fogel & Rutherford, 1995; Weitz et al., 1998).

Finally, our results show that for the range of H_2O and CO contents and compositions modeled here, the calculated mass flow rate was always between 3.4×10^6 and 6.7×10^6 kg s^{-1}. For the H_2 and CO model simulations, the mass flow rate showed similar values, ranging from 4.4×10^6 and 8.0×10^6 kg s^{-1} (see Table S4 in Supporting Information S1 for full results and details of all model simulations). The slightly lower solubility of H_2 compared with H_2O and its behavior of exsolving at greater depth result in a more buoyant magma. However, the results for the H_2O and CO model simulations do not differ greatly from the results of the H_2 and CO model simulations. The main differences are in the gas-slip velocity and the mass flow rate, differences that both appear to stem from the slightly lower solubility of H_2 in magma compared with H_2O.

3.2. Volatile Exsolution During Ascent

We now analyze the effect of the different initial volatile contents assumed on the exsolution of volatiles during ascent and on the resulting gas volume fractions. We present results for a yellow/intermediate-Ti picrite from 10 km (Figure 4) and 2 km (Figure 5) depth to the surface. For the model simulations concerning

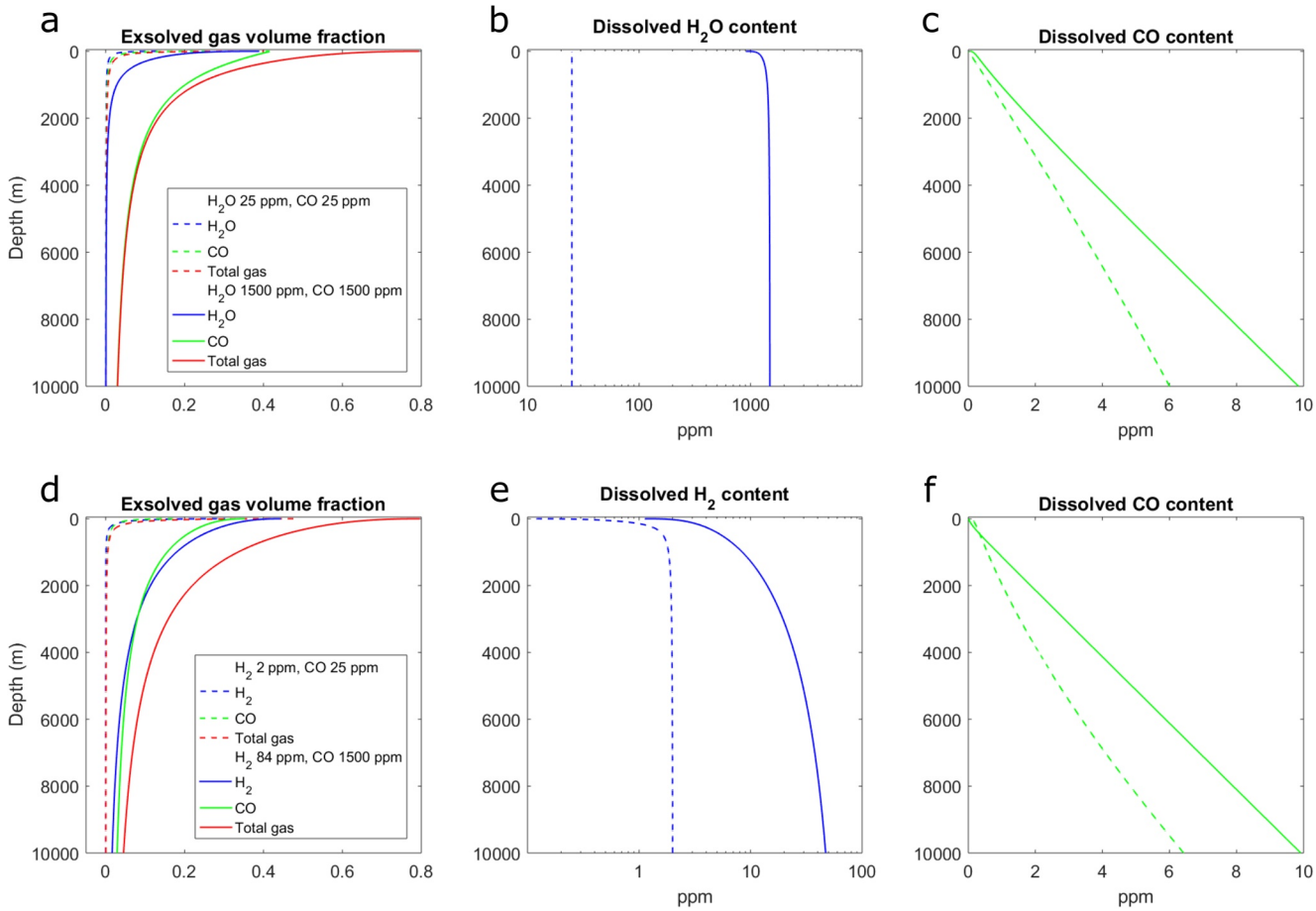

Figure 4. Volume fraction of exsolved gas and dissolved H_2O/H_2 and CO plots for a yellow/intermediate-Ti magma containing H_2O and CO (panels a–c) and H_2 and CO (panels d–f), all from a depth of 10 km to the surface. Dashed lines represent an initial volatile content of 25 ppm H_2O and 25 ppm CO, or 2 ppm H_2 and 25 ppm CO. Solid lines represent an initial volatile content of 1,500 ppm H_2O and 1,500 ppm CO, or 84 ppm H_2 and 1,500 ppm CO. Red lines represent the total volatile content, blue lines represent the H_2O or H_2 amount, and green lines represent the CO amount.

H_2O and CO, Figures 4a and 5a show that, for range of magma compositions and initial magmatic volatile contents modeled, CO made up the majority of the volume fraction of exsolved gas. For the low volatile content simulations, the total volume fraction of exsolved gas reaches 0.4 (Figures 4a and 5a, red dashed line), 70%–75% of which is CO. For the higher volatile content simulations, instead, the total exsolved gas volume fraction reaches 0.8 (Figures 4a and 5a, red solid line) at the vent of the conduit, 50%–55% of which is CO. However, for most of the conduit, CO is the dominant volatile species. These results are likely a product of the higher solubility of H_2O in magma compared with CO.

Results show that the amount of H_2O dissolved within the magma remains constant, except for when the high volatile content simulation reaches the upper 250 m of the conduit (Figure 4b). Meanwhile, most of the CO is already exsolved at 10 km depth, with only a small amount left dissolved in the melt (Figure 4c). This is a result of the low solubility of CO in lunar magmas. However, due to the high pressure, the exsolved CO volume fraction remains small until shallow depths (see green curves on Figures 4a and 5a).

The depth at which H_2O and CO exsolved showed little variation from very low- to high-Ti magma (Figures S1–S15 in Supporting Information S1); it appears that the magma compositions investigated here have little effect on the volume fraction of exsolved gas during ascent. The variation in major element composition does not seem to affect the solubility of the volatiles in the magma to a significant degree.

For the H_2 and CO model simulations, the role of both volatiles in driving magma ascent seems comparable, with H_2 being slightly more dominant for the low volatile content simulations (Figures 4d and 5b).

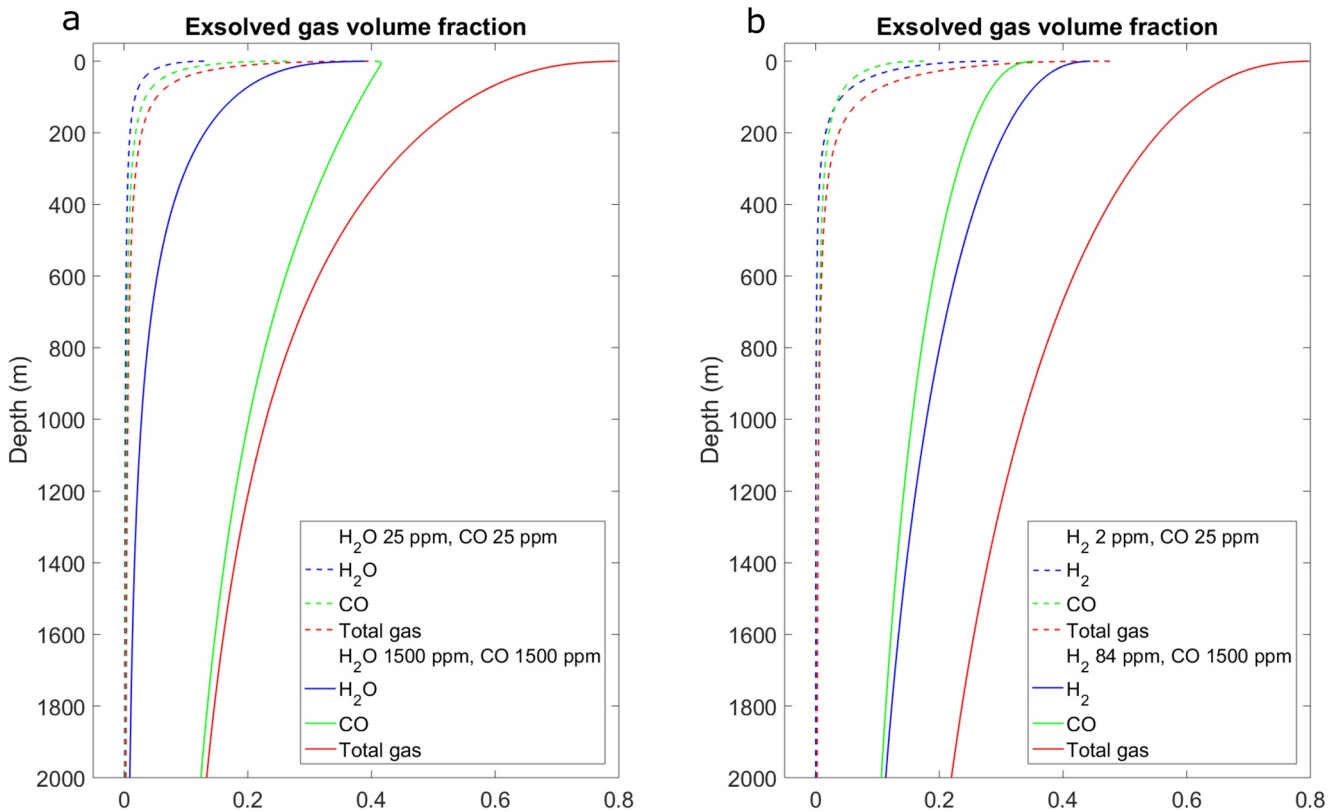

Figure 5. Volume fraction of exsolved gas and dissolved H_2O/H_2 and CO plots for a yellow/intermediate-Ti magma containing H_2O and CO (panel a) and H_2 and CO (panel b), from a depth of 2 km to the surface. Dashed lines represent an initial volatile content of 25 ppm H_2O and 25 ppm CO, or 2 ppm H_2 and 25 ppm CO. Solid lines represent an initial volatile content of 1,500 ppm H_2O and 1,500 ppm CO, or 84 ppm H_2 and 1,500 ppm CO. Red lines represent the total volatile content, blue lines represent the H_2O or H_2 amount, and green lines represent the CO amount.

Figure 4d shows that, for the low volatile content simulations, H_2 makes up 65%–70% of the total volume fraction of exsolved gas (0.5). For the high volatile content simulations, H_2 makes up 55%–60% of the total volume fraction of exsolved gas (0.8).

H_2 appears to be slightly less soluble in magma than H_2O, with H_2 exsolving more gradually between 10 and 2 km depth, compared with the more rapid exsolution of H_2O at shallow depths of 1–2 km (Figures 4b and 4d). Overall, these results show that, for the range of volatiles and volatile contents considered here, the dominant volatile that makes up the majority of the exsolved gas fraction is depending on which H-species is initially selected, giving a strong dependence on factors such as the oxygen fugacity of the system.

3.3. Sensitivity Analysis

The results of the sensitivity analysis have been illustrated with: plots showing frequency against selected output parameters (Figures 6 and 7); Sobol index plots (Figure 8); and correlation plots showing the relation between each volatile component against both exit velocity and exit pressure (Figures 9 and 10). The Sobol index of a given output parameter is a measure of how the variability in the output value is linked to the variability of different model inputs (La Spina et al., 2019). Therefore, the Sobol index can be used to comment on the relative influence of one input parameter (within the ranges investigated in the sensitivity analysis) on a specific output. The model inputs we analyzed were: pressure, temperature, conduit radius, H_2O or H_2 content, and CO content. The four model outputs we focus on are: exit gas volume fraction, mass flow rate, exit velocity, and exit pressure. We focus on results for a yellow/intermediate-Ti picrite for both the H_2 and CO and the H_2O and CO model simulations. For sensitivity analysis results for all picrite compositions, see Figures S16–S27 in Supporting Information S1.

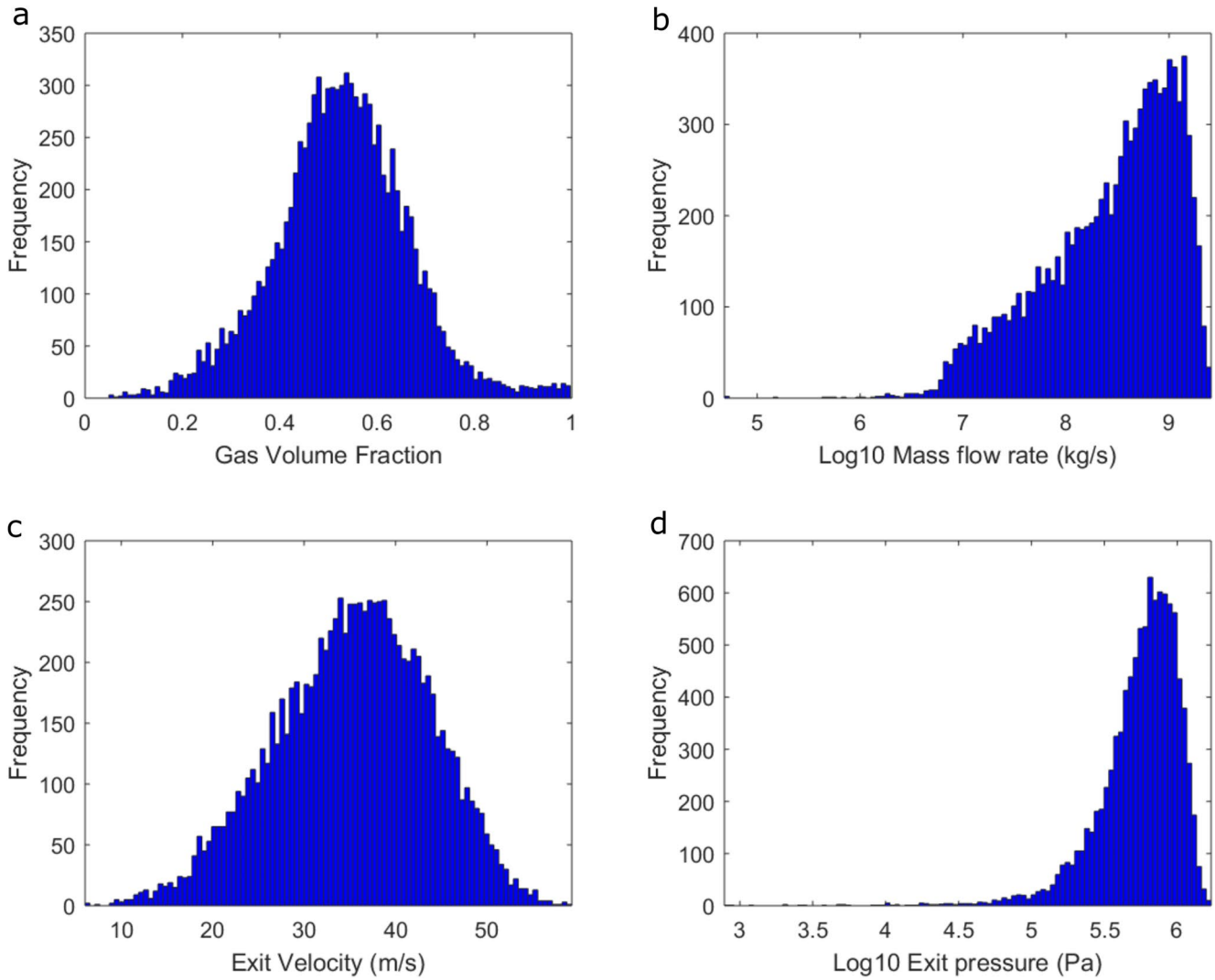

Figure 6. Frequency against selected output parameters obtained from the sensitivity analysis assuming a yellow/intermediate-Ti magma containing H_2O and CO: (a) exit gas volume fraction, (b) mass flow rate, (c) exit velocity, and (d) exit pressure.

Our results show that both mixtures of volatiles (H_2O-CO, and H_2-CO) produce a very similar exit gas volume fraction, mass flow rate, exit velocity, and exit pressure (Figures 6 and 7, Table 3). The only notable difference is that each of these model output parameters were consistently higher for the H_2-CO mixture, compared with the model simulations obtained assuming a H_2O-CO gas mixture by roughly 5%–10%.

The Sobol index plots (Figure 8) indicate that exit gas volume fraction was affected by all five input parameters tested. For the H_2O-CO model simulations, H_2O had a lower effect than that of CO. For the H_2-CO model simulations, instead, H_2 played a larger role than CO in affecting the gas volume fraction at the vent of the conduit. For both combinations of volatiles, mass flow rate was majorly controlled by conduit radius. For the H_2O-CO model simulations, CO was the dominant input parameter for controlling both exit velocity and exit pressure, with minimal contribution from H_2O. However, for the H_2-CO model simulations, H_2 and CO were roughly equal in terms of controlling the model output.

The significance of CO compared with H_2O can be seen in the correlation plots for exit velocity and pressure (Figure 9). These are illustrated in Figure 9 where each red point is the output value resulting from one simulation, whereas the blue line is the mean value of the outputs obtained for the given value of the corresponding input parameter. The higher the gradient of the blue line, the more significant the input

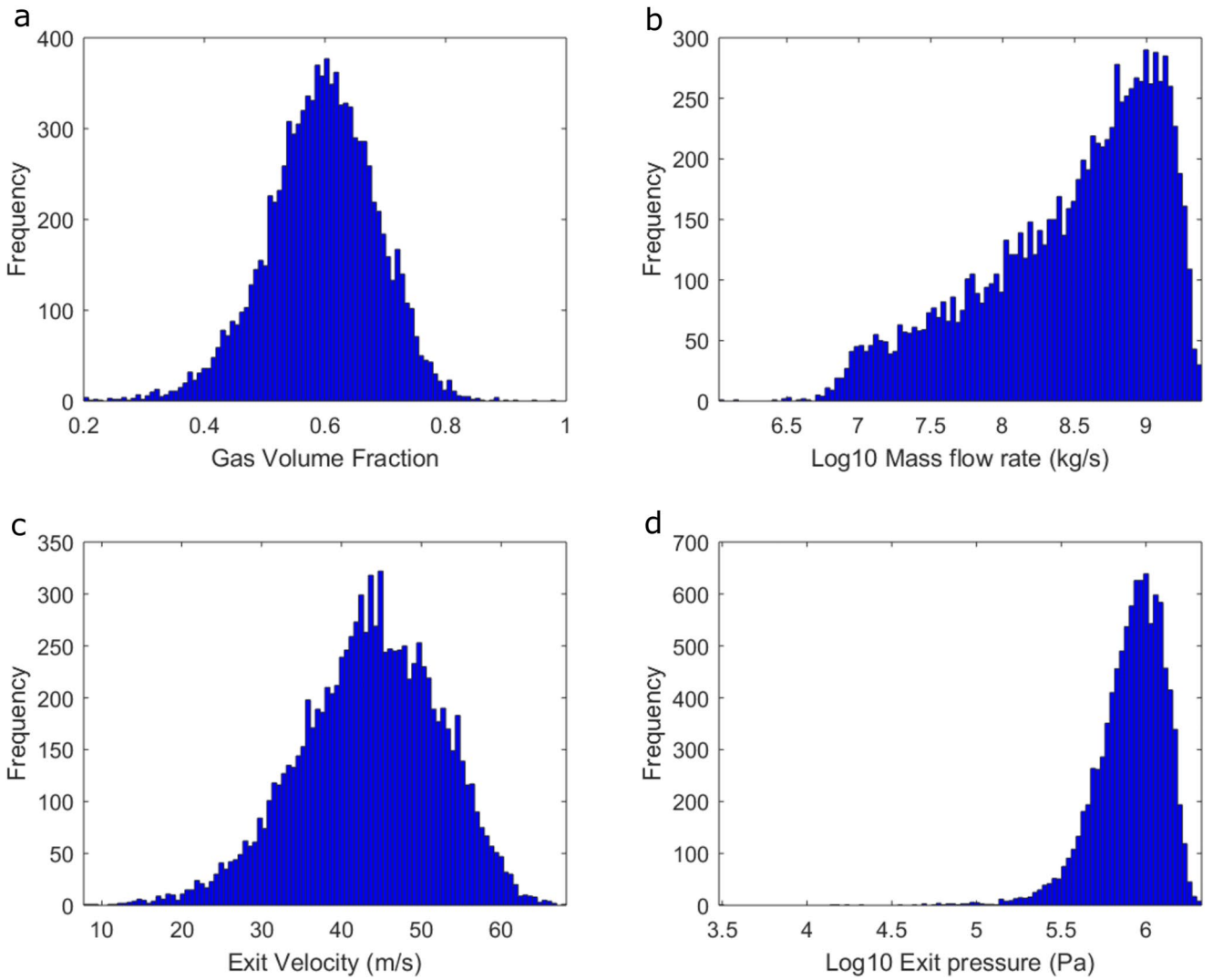

Figure 7. Frequency against selected output parameters obtained from the sensitivity analysis assuming a yellow/intermediate-Ti magma containing H_2 and CO: (a) exit gas volume fraction, (b) mass flow rate, (c) exit velocity, and (d) exit pressure.

Table 3
Summary of the Frequency Against Selected Output Parameters Graphs (Figures 6 and 7)

Output		H_2O and CO	H_2 and CO
Gas volume fraction	Range	0.05–0.95	0.20–0.95
	Peak	0.45–0.55	0.55–0.65
Mass flow rate (log 10 kg s^{-1})	Range	5.6–9.4	6.0–9.4
	Peak	8.5–9.0	8.8–9.2
Exit velocity (m s^{-1})	Range	6–60	8–67
	Peak	35–40	40–45
Exit pressure (log Pa)	Range	3.3–6.2	3.5–6.3
	Peak	5.7–6.0	5.9–6.1

parameter is for controlling the output. The blue lines for H_2O content are almost flat (Figures 9a and 9c), indicating that, across the H_2O contents investigated in the sensitivity analysis, H_2O is not affecting the exit velocity and exit pressure, confirming the findings of the Sobol index results. On the contrary, the gradient of the CO content curves is greater than that for H_2O, which indicates that CO has a greater influence on the calculated exit velocity and pressure (Figures 9b and 9d). This is likely to be a consequence of the relatively low initial H_2O content assumed and of the higher solubility of H_2O in magma compared to CO. Indeed, the combination of both results is an exsolution of H_2O only at very shallow depth, and thus water is not able to affect significantly the magma ascent dynamics. In Figure 10, we see that the gradient between H_2 and CO and exit velocity and exit pressure are very similar, suggesting that they have an equal effect on magma ascent dynamics.

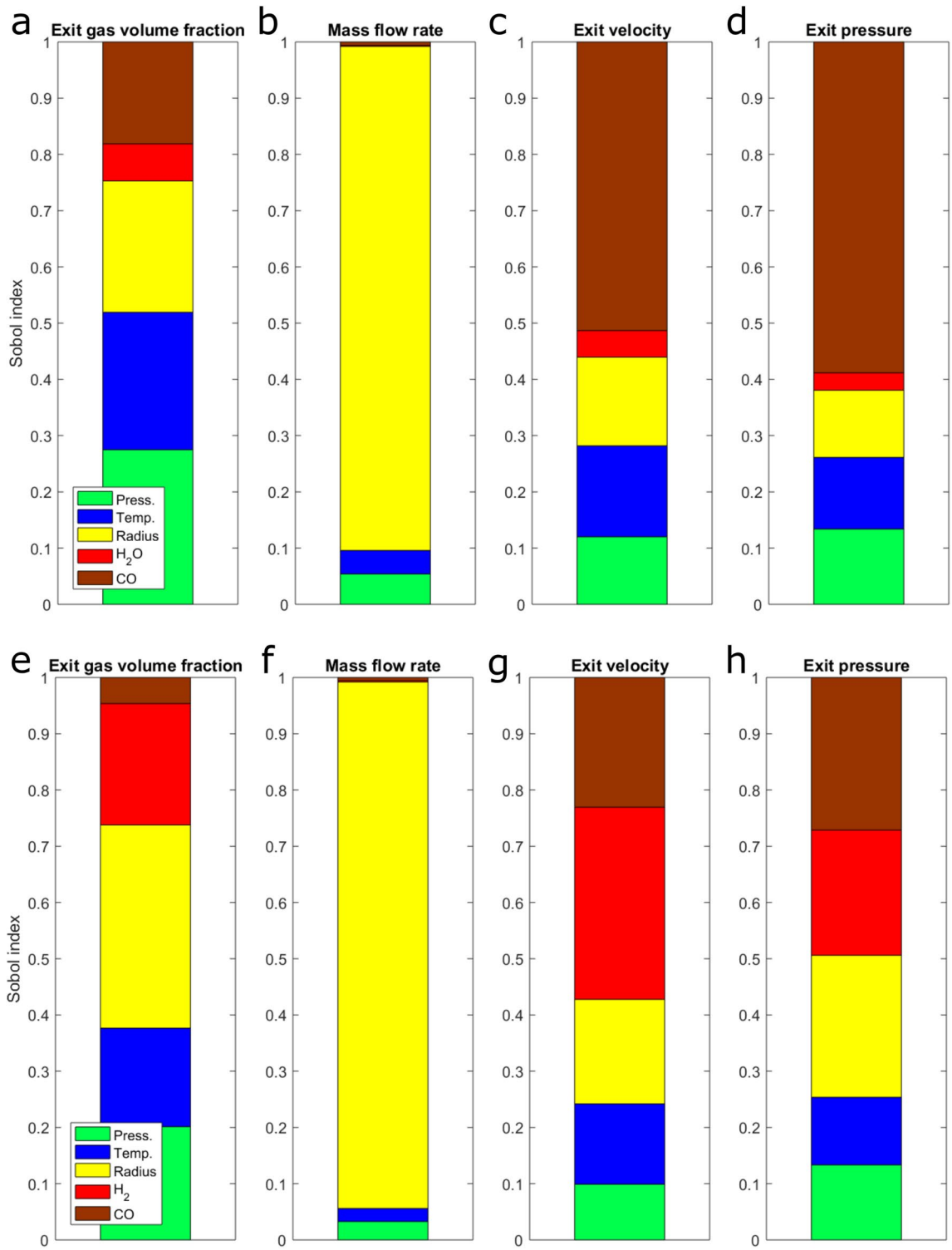

Figure 8. Sobol index plot obtained from the sensitivity analysis for yellow/intermediate-Ti magma containing H_2O and CO (panels a–d) and H_2 and CO (panels e–h), showing the relative important of pressure, temperature, conduit radius, initial H_2O content, and initial CO content on exit gas volume fraction (panels a and e), mass flow rate (panels b and f), exit velocity (panels c and g), and exit pressure (panels d and h). Results are based on 10,000 model simulations.

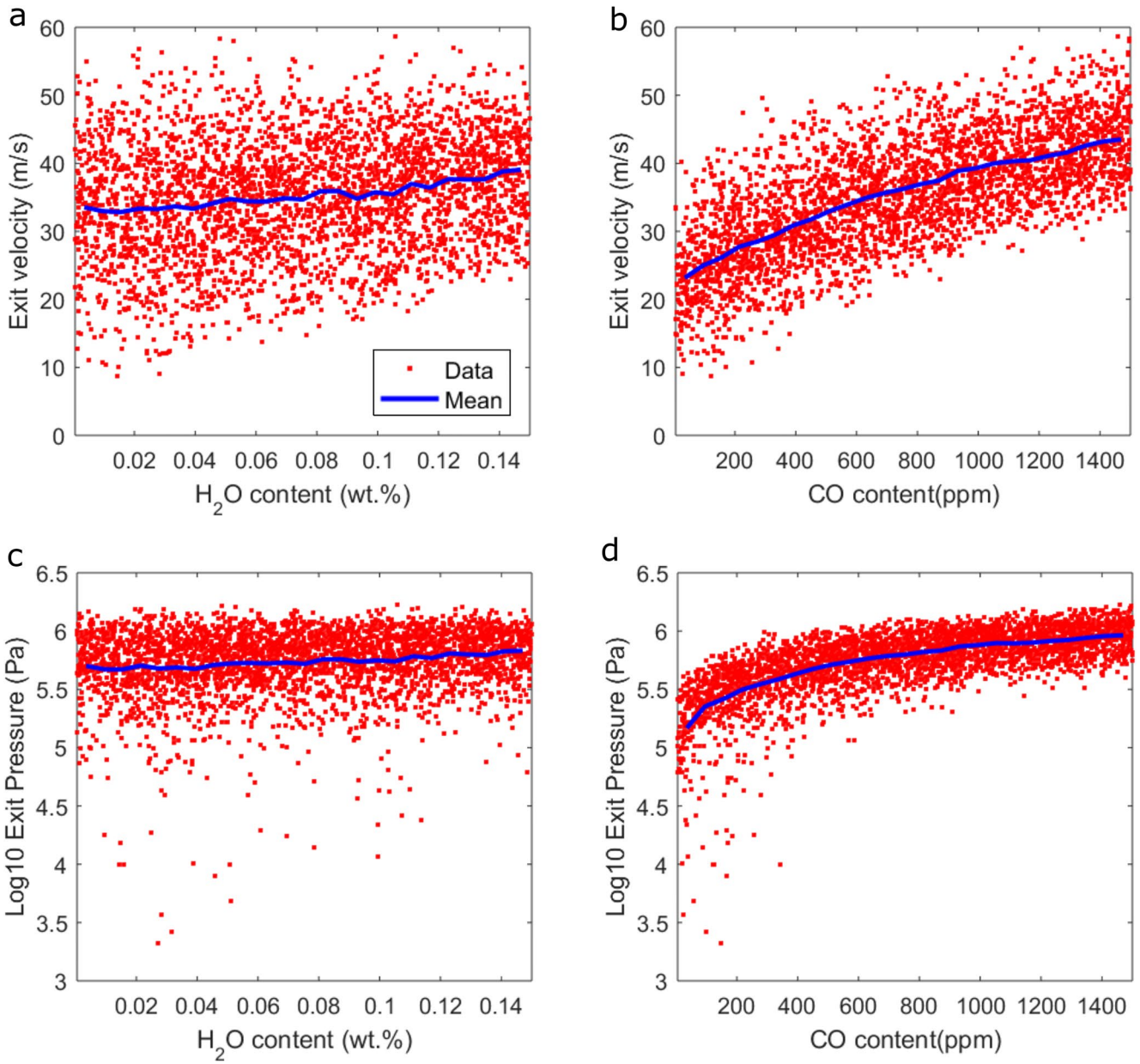

Figure 9. Correlation plots obtained from the sensitivity analysis for a yellow/intermediate-Ti picrite containing H_2O and CO, showing the variability of: exit velocity as function of (a) H_2O content, and (b) CO content; and exit pressure as function of (c) H_2O content, and (d) CO content. Each red point represents 1 of the 10,000 simulations. Each blue line represents the mean output value calculated for a given value of the input parameter. The gradient of each blue line indicates how strongly the input parameter affects the corresponding output parameter.

4. Discussion

4.1. Importance of Volatile Content and Composition on Magma Ascent Dynamics on the Moon

Our numerical modeling and sensitivity analysis results have shown that for a magma containing H_2O and CO, CO has a stronger control on lunar magma ascent dynamics than H_2O, for the range of initial volatile contents we investigated. Conversely, we have also shown that for a magma containing H_2 and CO, H_2 has a comparable or slightly stronger control on lunar magma ascent dynamics than CO.

According to our sensitivity analysis, for a magma containing H_2O and CO, initial CO content was the most significant input parameter controlling exit velocity and exit pressure (Figure 8), out of the input parameters analyzed. Initial CO content was also more significant than initial H_2O content for controlling the

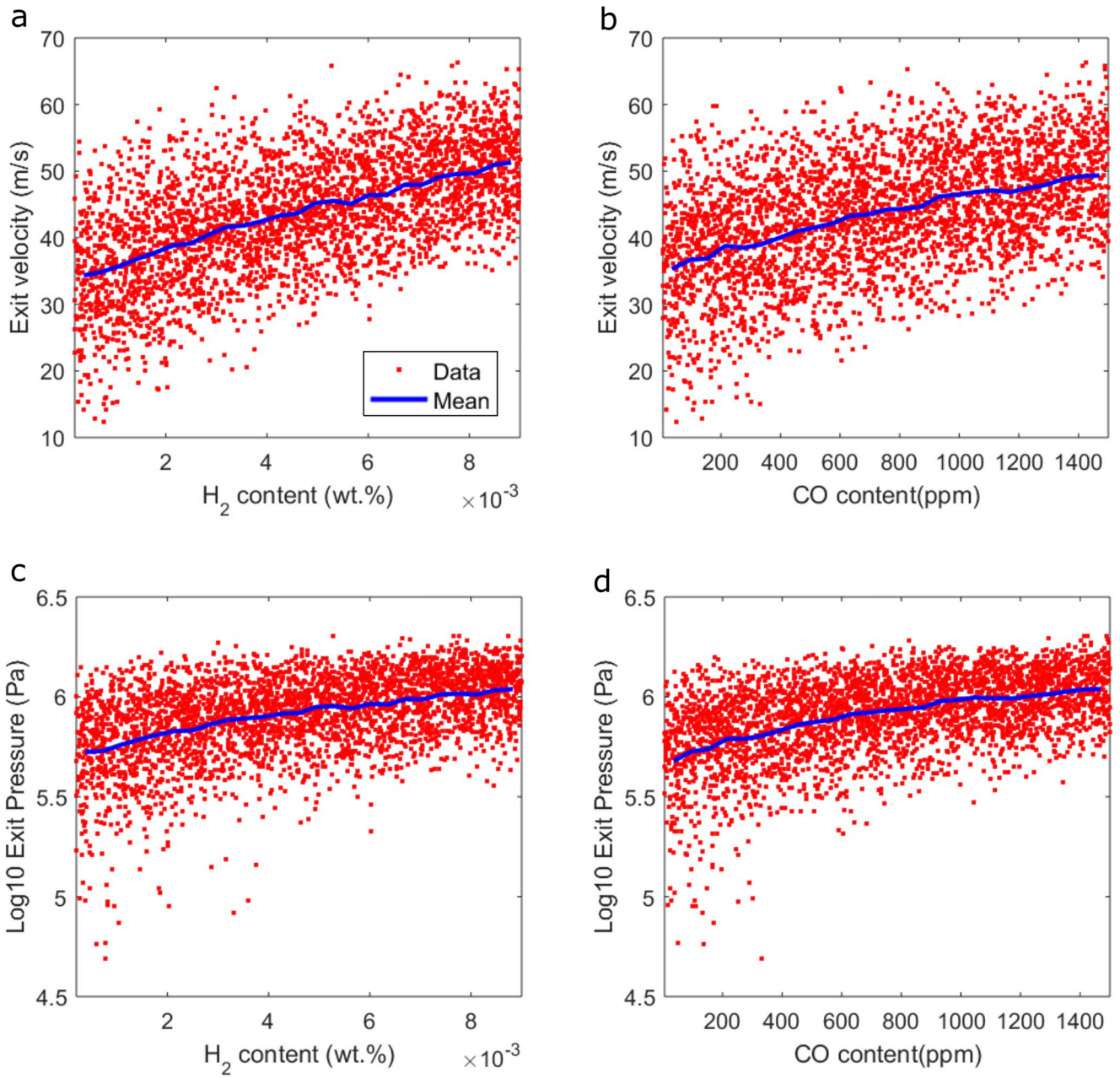

Figure 10. Correlation plots obtained from the sensitivity analysis for a yellow/intermediate-Ti picrite containing H_2 and CO, showing the variability of: exit velocity as function of (a) H_2 content, and (b) CO content; and exit pressure as function of (c) H_2 content, and (d) CO content. Each red point represents 1 of the 10,000 simulations. Each blue line represents the mean output value calculated for a given value of the input parameter. The gradient of each blue line indicates how strongly the input parameter affects the corresponding output parameter.

exsolved gas volume fraction, although initial pressure and temperature had a greater contribution than each of the volatiles. This result is in agreement with several previous studies that state that CO was a key volatile in driving lunar magma ascent and eruptions (Rutherford & Papale, 2009; Rutherford et al., 2017; Sato, 1979; Spera, 1992; Wilson & Head, 2017). For the simulated magma containing H_2 and CO, the sensitivity analysis results showed that H_2 content had a greater or roughly the same effect as CO content on the exit gas volume fraction, pressure, and velocity. Again, this is in agreement with recent studies that have considered H_2 to be a key volatile element in driving lunar magma ascent (McCubbin et al., 2015), although traces of H_2 have not yet been detected in the volatile-rich coatings on pyroclastic beads.

Since the initial CO and H_2 content of a magma (containing H_2O and CO or H_2 and CO respectively) has a strong control on the exit pressure and exit velocity, the initial CO or H_2 content must also have a significant degree of control on the shape of an eruption plume, eruption plume size, and the distances that pyroclasts would be ejected. With a greater exit gas volume fraction and exit pressure, we would expect that the later expansion of the eruption plume would be greater. According to Head and Wilson (2017), lunar volcanic plumes are made of a gas cloud, which expands hemispherically, and pyroclasts decoupled from the gas cloud, which disperse following ballistic trajectories. The wide-angle expansion of the gas cloud is the result of gas expansion in a vacuum. Furthermore, as the gas expands its density continues to decrease, until it is so small that the drag force on the pyroclasts becomes negligible (the critical gas density), and thus they decouple from the gas cloud following mainly ballistic trajectories. If a significant proportion of the pyroclasts are following a ballistic trajectory, a radial dispersal would be observed, ultimately creating a thin and widely dispersed pyroclastic deposit. However, before the critical gas density is reached, pyroclasts are affected by gas cloud expansion, and they are accelerated reaching velocities of several hundred of meters per second. The exit pressure and gas volume fraction at the vent of the conduit will affect the expansion of the gas cloud and the reaching of the critical gas density, influencing the pyroclasts ejection velocities, and ultimately the deposit.

Regarding magma fragmentation during ascent, our numerical results suggest that fragmentation would not occur within the conduit. The low and high volatile content simulations produced a similar Deborah number ($\sim 10^{-7}$), which was too low to reach the fragmentation threshold. Brittle or inertial fragmentation are likely to occur once magma is ejected from the vent, due to the strong acceleration that the magma will experience following the expansion of the gas cloud in the lunar vacuum. Which one of the two competing mechanisms is more likely to take place is difficult to forecast with our current numerical tool, and more appropriate modeling of this process is required. This would be also important to elucidate the role of the initial volatile content on magma fragmentation within a gas cloud. The link between initial volatile content and pyroclastic deposit morphology has recently been explored by Morgan et al. (2021), using measurements of volatile abundance and release patterns from experiments to estimate pyroclast grain size distributions and their subsequent ejection distances. Their results predicted a bimodal pyroclastic grain size distribution, a maximum pyroclast ejection distance of 20 km (a distance that encompasses 79% of all observed lunar pyroclastic deposits), and that a wide range of volatile contents are responsible for producing the wide range of deposit sizes observed. Future developments could involve utilizing the magma ascent model results in the context of the Morgan et al. (2021) work.

We can also comment on the effect of different compositions on magma ascent dynamics, since we modeled the full range of picritic compositions from a green/very low-Ti to a black/high-Ti picrite. The magmatic major element compositions investigated here seem to not have a significant effect on the overall magma ascent dynamics. As expected, the only parameter that appears to be affected by magma composition is viscosity, with an order of magnitude difference between the green/VLT picrite (viscosity of ~1 Pa s) to the black/high-Ti picrite (viscosity of ~10 Pa s). This variation in viscosity is not enough to produce a significant effect on magma ascent dynamics and, thus, the simulations obtained with the different compositions are very similar to one another (Figures 1 and 2).

It is important to highlight that we have tested a range of initial volatile contents based on measurements and modeled values from returned samples of lunar picritic glass beads (Saal et al., 2008; Wetzel et al., 2015), supplemented by data from terrestrial volcanic systems where there is limited data on lunar volcanic systems (Gerlach et al., 2002; Hekinian et al., 2000). Therefore, any errors or uncertainties associated with these measurements are carried forward to our results.

Finally, we modeled the ascent of a magma containing combinations of H_2 and CO (to represent the most likely H- and C-species, based on geochemical conditions present in the lunar mantle) and H_2O and CO (to utilize the plethora of information available on the behavior of H_2O in silicate melts). The results of the two different modeling scenarios show opposing results in terms of whether an H- or C-species is dominating magma ascent and eruption dynamics. We cannot be sure which of the two different modeling scenarios are more accurate, since the exact proportions in which H would partition into H_2O and H_2 at 10 km depth within the lunar mantle are not fully understood. Renggli et al. (2017) highlighted the importance of redox conditions in controlling H speciation, while Hirschmann et al. (2012) also demonstrated the importance of

pressure and magmatic H_2 content on H speciation. Hirschmann et al. (2012) calculated that, for a magma containing 1,000 ppm H_2 at a pressure of 0.1 GPa (i.e., conditions on the same order of magnitude as this study), the molar ratio of H_2 within a magma would be 10%–30%. The molar ratio of H_2 within a melt only exceeds 50% for a magma containing >2,000 ppm H_2 at >3 GPa, suggesting that, for the pressure conditions simulated in this study, H_2O would be the dominant H-species in the magma. Overall, the results from this study highlight the importance of factors such as melt system oxygen fugacity, H content, and pressure in understanding how H partitions between H_2O and H_2 in magmas, and, therefore, how different volatile elements control magma ascent and eruption.

4.2. Comparison With Results From Previous Magma Ascent Models and Experiments

We compare our findings with results from previous numerical and experimental models (Rutherford & Papale, 2009; Rutherford et al., 2017; Wilson & Head, 2018). Our sensitivity analysis showed that, across all initial volatile contents and compositions, exit mixture velocity varied from 5 to 60 m s^{-1}, with a peak in the middle of this range at 25–35 m s^{-1}. These results match previous estimates for average ascent velocity of 20–30 m s^{-1} (Wilson & Head, 2018), and previous estimates for exit mixture velocity between 15 and 35 m s^{-1} (Rutherford & Papale, 2009). This is useful for understanding the conditions and style with which the picritic glass beads erupted, such as eruption height and pyroclast dispersal distance, although calculating these conditions is beyond the scope of this work.

Rutherford et al. (2017) devised a model for the ascent of high-Ti/orange picritic magma, based on gas solubility experiments. High-temperature and -pressure experiments were used to simulate magma ascent, in order to determine the type and abundance of volatile species that would exsolve during the ascent of an analogue orange picrite. Matching depth in the conduit with the corresponding temperature and pressure, three stages of lunar magma ascent were interpreted: (a) 550 km depth, the source region of the picrite partial melt zone, up to 50 km depth, (b) 50–0.5 km depth: C, O, H, and S compounds exsolve from the magma, and (c) < 500 m depth: volatile phases continue to exsolve within a closed system, with a gas volume fraction of 0.7 at a depth of ~130 m. While we only model to a depth of 10 km, it can be said that our results partly match the gas volume fraction measured for stage 3 of the Rutherford et al. (2017) model; indeed, we see an exit gas volume fraction of 0.7–0.8 for an intermediate-Ti, high volatile content simulations (Figures 3d and 4b). However, they conclude that fragmentation would take place at a depth of 130 m, based on the reaching of a critical gas volume fraction (0.7) (Sparks, 1978), or at a depth of 300–600 m, based on the pressure required to explain the carbon content of the samples. Differences with the Rutherford et al. (2017) model likely stem from the different initial volatile contents utilized (800–900 ppm H_2O and 1,280 ppm CO) and from the different fragmentation models incorporated. Our results suggest, based on the pressure and choked flow conditions and the Deborah number, that fragmentation would occur once the magma exits the vent, which is in agreement with the conclusions made by Rutherford and Papale (2009).

The distinction of lava fountaining as a separate eruption style from effusive and explosive activity in terrestrial basaltic eruptions has recently been made by La Spina et al. (2021). They show that for a lava fountaining eruption style, fragmentation does not occur within the conduit, but above the vent. Our results are consistent with previous models that attribute the lunar pyroclastic glass beads to lava fountaining (Carter et al., 2009; Coombs & Hawke, 1992; Elkins-Tanton et al., 2003a), but also match the recent work that quantitatively defines lava fountaining behavior on Earth (La Spina et al., 2021). Understanding the volume fractions of gas present during ascent and eruption, as well as the point at which fragmentation occurs, is important for understanding the emplacement of lunar pyroclastic deposits, in particular the size distribution of pyroclasts and the extent of different deposits.

4.3. Comparison With Volcanism on Other Planetary Bodies

Many questions still exist regarding the volatile budget and style of volcanic activity across the silicate bodies in our solar system (Horowitz et al., 2017; McCubbin et al., 2015; Tartèse et al., 2013). The surfaces of our Moon, Mercury, and Mars have been well imaged by various satellites, allowing us to make measurements of various volcanic features on these bodies, such as lava flows and pyroclastic deposits. From this, some

inferences have been made on the volatile content of the different magmas that drove volcanic activity, which have been paired with geochemical information to understand the volatile species that may have been present. We briefly detail some of the progress that has been made in understanding the volatiles that may have driven volcanism on Mercury and Mars, to put our work into context.

4.3.1. Mercury

Over 50 deposits mapped on Mercury's surface are thought to have been produced by explosive volcanic activity (Goudge et al., 2014). Mercurian pyroclastic deposits generally have a greater areal extent than lunar pyroclastic deposits, which has led to the inference that Mercury's pyroclastic eruptions involved greater amounts of volatiles than lunar pyroclastic eruptions (Kerber et al., 2011). Based on the age-relationships between pyroclastic deposits and impact craters, Thomas et al. (2014) suggested that long-lived explosive volcanism occurred on Mercury, spanning from ~3.9 to 1.0 Ga. Not only does this provide information on the thermal history of Mercury, it also indicates that Mercury had a relatively substantial mantle volatile inventory. Based on the highly reducing conditions likely present, it is unlikely that H_2O is abundant in Mercury's mantle (Hirschmann et al., 2012). Several volatiles have been proposed as the main drivers of Mercury's explosive volcanic activity: S_2Cl, Cl, Cl_2, and COS (Kerber et al., 2011), as well as H_2 and H_2S (Greenwood et al., 2018). These studies verified results from a chemical equilibrium model by Zolotov (2010), which suggested that N_2, CO, S_2, CS_2, S_2Cl, Cl, Cl_2, and COS could make up a significant portion of Mercury's volcanic gases.

To give a sense of scale between our results and pyroclastic deposits on Mercury, we give a brief comparison with a study by Kerber et al. (2009a, 2009b). Based on the morphology of a large volcanic deposit in the Caloris impact basin, Kerber et al. (2009a, 2009b) calculated the minimum vent speed and volatile content required to eject a pyroclast 24 km (the radius of the Caloris basin pyroclastic deposit) from the vent. They calculated that a minimum exit velocity of 300 m s^{-1} and volatile abundances of 3,600 ppm H_2O and 5,500 ppm CO, which they calculated to be the equivalent of 1,600 ppm of H_2O and 2,400 ppm of CO in lunar conditions. This suggests that the volatile contents we modeled, which are based on measured and modeled volatile abundances in lunar samples, would not propel pyroclasts to distances as far as the 24 km measured for the Caloris basin pyroclastic deposit.

4.3.2. Mars

The majority of volcanic deposits on Mars that have been studied have been produced by effusive volcanic activity (Glaze & Baloga, 2006; Hulme, 1976; Wilson et al., 2009). Although there are a growing number of studies looking at more cone-like deposits, produced by explosive activity (Brož & Hauber, 2011; Lanz et al., 2010), there are still many connections to be made between studies of volatiles in Mars' mantle (such as Filiberto & Treiman, 2009; Filiberto et al., 2016), and understanding the key volatile elements that drove explosive volcanic activity on Mars.

Compared with Mercury, a much greater wealth of information on the volatile content and oxygen fugacity of the Martian interior exists due to studies of Martian meteorites. The main volatiles that have been studied include H_2O, C-species, S-species, F, and Cl. For H_2O, there has been some debate over whether Martian meteorites are anhydrous (Leshin et al., 1996) or whether they represent material that has completely degassed during eruption or emplacement (McSween et al., 2001; Nekvasil et al., 2007). A generally accepted value of 73–290 ppm H_2O in the Martian mantle has been estimated from apatites found in shergottites (McCubbin et al., 2012), which is on the same order of magnitude as current lunar estimates (Boyce et al., 2010; Tartèse et al., 2013; Wang et al., 2012). Based on geochemical and experimental constraints, it has also been suggested that Cl and F were more abundant than H_2O in Martian magmas, and therefore may have had a greater influence on driving magma ascent and eruption (Filiberto et al., 2016; Filiberto & Treiman, 2009).

4.4. Future Model Applications and Developments

The links between volcanic deposit morphology and eruption conditions have been well explored for a range of planetary bodies and features (Garry et al., 2007; Lena et al., 2008; H. J. Moore et al., 1978; Wilson et al., 2009). For the results presented here, we suggest that the calculated mass flow rates (Table S4 in Supporting Information S1) could be paired with measurements of the volumes of pyroclastic deposits (such as Trang et al., 2017) to provide some estimates on the duration of eruptions on the Moon, which is poorly

understood. Such knowledge could provide useful insight into the repose time between periods of volatile release on the lunar surface, helping to understand whether transient atmosphere(s) existed on the Moon during periods of regular or pronounced volcanic activity (Head et al., 2020; Needham & Kring, 2017). The results of our sensitivity analysis showed that conduit radius had a very strong control on the calculated mass eruption rate. Therefore, in order to produce these robust estimates for eruption duration, the range of values used for the conduit radius would need to be constrained with better certainty. At present, it has not been possible to resolve individual magmatic conduits from lunar gravimetric data (Andrews-Hanna et al., 2013); as more data becomes available, this avenue could be explored more effectively.

There are several different aspects of lunar volcanism that could be investigated using the magma ascent model used here. First of all, the ascent of high-Ti basalts could be investigated in more detail. Although it is assumed that partial melts within the lunar crust would always buoyantly ascend due to a sufficient density difference, Delano (1990) proposed that high-Ti basalts would be an exception to this rule, calculating that high-Ti basalts would exceed a "compositional limit of eruptability." Delano (1990) calculated that a TiO_2 content of roughly 16.4% would result in such a high density that any dykes would stall or even descend within the mantle or crust. This value for TiO_2 content is difficult to verify: if samples of this magma are not reaching the surface due to stalling, then there is an inherent bias in samples of picritic glass beads, samples which we must base our modeled compositions on (Shearer et al., 1990). While we used the same density for all compositions of magma within the equations of state of the model, the magma ascent model used here would be a fitting method for investigating the initial conditions that would produce a theoretical limit, beyond which a magma would not ascend and erupt.

Second, data from future missions could be used to infer the magma ascent model to understand specific volcanic sites on the Moon, for example, samples collected by Chang'e 5 from northern Oceanus Procellarum. Compositional data could provide information for the initial conditions of the magma ascent model, which could be used to simulate magma ascent in the area. This could be particularly useful since the basalts near Chang'e 5's landing site are thought to be some of the youngest mare basalts, with some areas of high-Ti basalt present (Qian et al., 2021).

5. Conclusions

We have investigated the effect of different magmatic H- and C-species and volatile contents on magma ascent dynamics, for the ascent of picritic magma within the lunar crust. We have applied a 1-dimensional, multiphase numerical model, previously used for terrestrial cases (de' Michieli Vitturi et al., 2011; La Spina et al., 2015, 2016, 2017, 2019, 2021) to a lunar scenario. We also performed a sensitivity analysis to investigate the relationship between various initial conditions and model outputs.

Using measured and modeled H_2, H_2O, and CO abundances in the numerical magma ascent model and sensitivity analysis, we have shown that CO has a stronger control on the magma ascent dynamics than H_2O, for model simulations investigating H_2O and CO. We can see from gas exsolution profiles and Sobol indices that the range of H_2O abundances presented in previous studies (Saal et al., 2008) do not have a large effect on magma ascent dynamics compared with other initial conditions, namely CO abundance, temperature, pressure, and conduit radius. Initial CO content had the strongest control on exit velocity and exit pressure, which, in turn, strongly influence the formation of plumes, ejection of ballistics in the surrounding area, and, ultimately, the deposits that we can observe on the surface of the Moon. It is likely that initial CO content has a significant control on eruption style and eventual pyroclastic deposit morphology, making it a key volatile for driving lunar volcanic eruptions. This finding is in agreement with a number of studies (Rutherford & Papale, 2009; Rutherford et al., 2017; Sato, 1979; Wilson & Head, 2017). We conclude that understanding the abundance and origin of CO is of great importance for understanding lunar magma ascent, subsequent eruption processes, and deposit morphology.

For model simulations investigating H_2 and CO, we have shown that H_2 has a similar or slightly greater control on magma ascent dynamics than CO. While some authors have suggested that H_2 would be the dominant H-species driving lunar magma ascent and eruption (Renggli et al., 2017), other studies have shown that H_2O would be the more abundant H-species present for the conditions simulated in our magma ascent model (Hirschmann et al., 2012). Overall, the results from this study highlight the importance of factors such as oxygen fugacity, H content, and pressure in understanding how H partitions between H_2O and H_2 in

magmas, and therefore, how different volatile elements control magma ascent and eruption. In any case, for the ranges of volatile abundances considered here, either H_2 or H_2O produce similar values (i.e., results for H_2 only 5%–10% higher than for H_2O) for mass eruption rate, exit velocity, exit pressure, and exit gas volume fraction, suggesting that the differences in plume dispersal or ballistic ejection would not be significant.

Our results also showed that magma composition does not have a significant effect on the overall magma ascent dynamics. The different compositions adopted affect the magma viscosity, with an order of magnitude difference between the green/very low-Ti picrite (viscosity of ∼1 Pa s) to the black/high-Ti picrite (viscosity of ∼10 Pa s). However, this variation in viscosity is not enough to produce a significant variation in the magma ascent dynamics across the different magmas, and thus differences in magma composition are unlikely to produce significant differences in eruption style.

The methods used in this study could provide a wealth of information on many different aspects of lunar volcanism, such as understanding lunar eruption processes in a quantitative way, the role of different S-species in driving lunar eruptions, or the feasibility of the ascent of high-Ti magmas. The application of increasingly sophisticated numerical models of magma ascent to investigate planetary volcanism will only increase over time as more data (such as the interior compositions, magmatic compositions, and volatile contents across different planetary bodies) becomes available to the scientific community.

Conflict of Interest

The authors declare no conflicts of interest relevant to this study

Data Availability Statement

The magma ascent model used in this study is adapted from the MAMMA model, available on GitHub https://github.com/demichie/MAMMA. The data associated with the paper is available on Figshare and will be stored there publicly and permanently if the publication is accepted: Lo et al. (2021): Data for "Determining the effect of varying magmatic volatile content on lunar magma ascent dynamics." University of Manchester. Collection. https://doi.org/10.48420/c.5557635.v1.

Acknowledgments
M. Lo thanks support from an STFC studentship (ST/S505560/1). K. H. Joy thanks STFC (ST/M001253/1), the Royal Society (URF\R\201009), and the Leverhulme Trust (RPG-2019-222) for support. Contributions of G. La Spina, M. Polacci, and M. Burton have been supported by funding from RCUK NERC DisEqm project (NE/N018575/1). The authors would like to thank two anonymous reviewers for their constructive and helpful reviews and Editor Laurent Montesi for their help with editorial handling.

References

Adams, B. M., Bohnhoff, W. J., Dalbey, K. R., Ebeida, M. S., Eddy, J. P., Eldred, M. S., et al. (2014). *Dakota, a multilevel parallel object-oriented framework for design optimization, parameter estimation, uncertainty quantification, and sensitivity analysis. (Version 6.11 user's manual. Sandia technical report SAND2014-4633).* Albuquerque, New Mexico: Sandia National Laboratories. https://doi.org/10.2172/1177077

Anand, M., Tartèse, R., & Barnes, J. J. (2014). Understanding the origin and evolution of water in the Moon through lunar sample studies. *Philosophical Transactions of the Royal Society A*, *372*, 20130254. https://doi.org/10.1098/rsta.2013.0254

Anderson, E. M. (1951). *The dynamics of faulting and dyke formation with applications to Britain*. Oliver and Boyd.

Andrews-Hanna, J. C., Asmar, S. W., Head, J. W., Kiefer, W. S., Konopliv, A. S., Lemoine, F. G., et al. (2013). Ancient igneous intrusions and early expansion of the Moon revealed by GRAIL gravity gradiometry. *Science*, *93*, 675–678. https://doi.org/10.1126/science.1231753

Aravena, Á., de' Michieli Vitturi, M., Cioni, R., & Neri, A. (2017). Stability of volcanic conduits during explosive eruptions. *Journal of Volcanology and Geothermal Research*, *339*, 52–62. https://doi.org/10.1016/j.jvolgeores.2017.05.003

Aravena, Á., de' Michieli Vitturi, M., Cioni, R., & Neri, A. (2018). Physical constraints for effective magma-water interaction along volcanic conduits during silicic explosive eruptions. *Geology*, *46*(10), 867–870. https://doi.org/10.1130/G45065.1

Arzilli, F., La Spina, G., Burton, M. R., Polacci, M., Gall, N. L., Hartley, M. E., et al. (2019). Magma fragmentation in highly explosive basaltic eruptions induced by rapid crystallization. *Nature Geoscience*, *10*, 1023–1028. https://doi.org/10.1038/s41561-019-0468-6

Basaltic Volcanism Study Project. (1981). *Basaltic volcanism on the terrestrial Planets*. Pergamon Press Inc.

Binder, A. B. (1976). On the compositions and characteristics of the mare basalt magmas and their source regions. *The Moon*, *16*(1), 115–150. https://doi.org/10.1007/bf00648049

Blundy, J., Cashman, K., & Humphreys, M. (2006). Magma heating by decompression-driven crystallization beneath andesite volcanoes. *Nature*, *443*, 76–80. https://doi.org/10.1038/nature05100

Boyce, J. W., Liu, Y., Rossman, G. R., Guan, Y., Eiler, J. M., Stolper, E. M., & Taylor, L. A. (2010). Lunar apatite with terrestrial volatile abundances. *Nature*, *466*(7305), 466–469. https://doi.org/10.1038/nature09274

Braden, S. E., Stopar, J. D., Robinson, M. S., Lawrence, S. J., Van Der Bogert, C. H., & Hiesinger, H. (2014). Evidence for basaltic volcanism on the Moon within the past 100 million years. *Nature Geoscience*, *7*(11), 787–791. https://doi.org/10.1038/ngeo2252

Brown, S. M., & Grove, T. L. (2015). Origin of the Apollo 14, 15, and 17 yellow ultramafic glasses by mixing of deep cumulate remelts. *Geochimica et Cosmochimica Acta*, *171*, 201–215. https://doi.org/10.1016/j.gca.2015.09.001

Brož, P., & Hauber, E. (2011). A unique volcanic field in Tharsis, Mars: Pyroclastic cones as evidence for explosive eruptions. *Icarus*, *218*, 88–99. https://doi.org/10.1016/j.icarus.2011.11.030

Caricchi, L., Burlini, L., Ulmer, P., Gerya, T., Vassalli, M., & Papale, P. (2007). Non-Newtonian rheology of crystal-bearing magmas and implications for magma ascent dynamics. *Earth and Planetary Science Letters*, *264*, 402–419. https://doi.org/10.1016/j.epsl.2007.09.032

Carr, B. B., Clarke, A. B., & de' Michieli Vitturi, M. (2018). Earthquake induced variations in extrusion rate: A numerical modeling approach to the 2006 eruption of Merapi Volcano (Indonesia). *Earth and Planetary Science Letters*, *482*, 377–387. https://doi.org/10.1016/j.epsl.2017.11.019

Carter, L. M., Campbell, B. A., Hawke, B. R., Campbell, D. B., & Nolan, M. C. (2009). Radar remote sensing of pyroclastic deposits in the southern Mare Serenitatis and Mare Vaporum regions of the Moon. *Journal of Geophysical Research*, *114*, 1–12. https://doi.org/10.1029/2009JE003406

Colebrook, F. (1939). Turbulent flow in pipes with particular reference to the transition region between the smooth and rough pipe laws. *Journal of the Institution of Civil Engineers*, *4*, 14–25. https://doi.org/10.1680/ijoti.1939.13150

Coombs, C., & Hawke, B. R. (1992). Pyroclastic deposits on the western limb of the Moon. In *Proceedings of the lunar and planetary science conference* (pp. 303–312). Lunar and Planetary Institute.

Costa, A. (2005). Viscosity of high crystal content melts: Dependence on solid fraction. *Geophysical Research Letters*, *32*, L22308. https://doi.org/10.1029/2005GL024303

Costa, A., Caricchi, L., & Bagdassarov, N. (2009). A model for the rheology of particle-bearing suspensions and partially molten rocks. *Geochemistry, Geophysics, Geosystems*, *10*, Q03010. https://doi.org/10.1029/2008GC002138

Costa, A. L., Melnik, O., & Vedeneeva, E. (2007). Thermal effects during magma ascent in conduits. *Journal of Geophysical Research*, *112*, B12205. https://doi.org/10.1029/2007JB004985

de' Michieli Vitturi, M., Clarke, A. B., Neri, A., & Voight, B. (2008). Effects of conduit geometry on magma ascent dynamics in dome-forming eruptions. *Earth and Planetary Science Letters*, *272*(3–4), 567–578. https://doi.org/10.1016/j.epsl.2008.05.025

de' Michieli Vitturi, M., Clarke, A. B., Neri, A., & Voight, B. (2010). Transient effects of magma ascent dynamics along a geometrically variable dome-feeding conduit. *Earth and Planetary Science Letters*, *295*, 541–553. https://doi.org/10.1016/j.epsl.2010.04.029

de' Michieli Vitturi, M., Clarke, A. B., Neri, A., & Voight, B. (2011). Assessing the influence of disequilibrium crystallization and degassing during magma ascent in effusive and explosive eruptions (#V23H-05). *Paper presented at American Geophysical Union Fall Meeting*. San Francisco, California, United States.

Degruyter, W., Bachmann, O., Burgisser, A., & Manga, M. (2012). The effects of outgassing on the transition between effusive and explosive silicic eruptions. *Earth and Planetary Science Letters*, *349–350*, 161–170. https://doi.org/10.1016/j.epsl.2012.06.056

Delano, J. W. (1980). Chemistry and liquidus phase relations of Apollo 15 red glass: Implications for the deep lunar interior. In *Proceedings of the lunar and planetary science conference* (pp. 251–288). Lunar and Planetary Institute.

Delano, J. W. (1986). Pristine lunar glasses: Criteria, data, and implications. *Journal of Geophysical Research*, *91*(B4), 201–213. https://doi.org/10.1029/JB091iB04p0D201

Delano, J. W. (1990). Buoyancy-driven melt segregation in the Earth's Moon, I. Numerical results. In *Proceedings of the lunar and planetary science conference* (pp. 3–12). Lunar and Planetary Institute.

Delano, J. W., & Lindsley, D. H. (1983). Mare glasses from Apollo 17: Constraints on the Moon's bulk composition. In *Proceedings of the lunar and planetary science conference* (pp. B3–B16). Lunar and Planetary Institute. https://doi.org/10.1029/jb088is01p000b3

Delano, J. W., & Livi, K. (1981). Lunar volcanic glasses and their constraints on mare petrogenesis. *Geochimica et Cosmochimica Acta*, *45*, 2137–2149. https://doi.org/10.1016/0016-7037(81)90066-1

Dingwell, D. B., & Webb, S. L. (1989). Structural relaxation in silicate melts and non-Newtonian melt rheology in geologic processes. *Physics and Chemistry of Minerals*, *16*, 508–516. https://doi.org/10.1007/BF00197020

Elkins-Tanton, L. T., Chatterjee, N., & Grove, T. L. (2003a). Magmatic processes that produced lunar fire fountains. *Geophysical Research Letters*, *30*(10), D505–D508. https://doi.org/10.1029/2003GL017082

Elkins-Tanton, L. T., Chatterjee, N., & Grove, T. L. (2003b). Experimental and petrological constraints on lunar differentiation from the Apollo 15 green picritic glasses. *Meteoritics & Planetary Sciences*, *38*(4), 515–527. https://doi.org/10.1111/j.1945-5100.2003.tb00024.x

Fang, X., Xu, Y., & Zhou, Z. (2011). New correlations of single-phase friction factor for turbulent pipe flow and evaluation of existing single-phase friction factor correlations. *Nuclear Engineering and Design*, *241*, 897–902. https://doi.org/10.1016/j.nucengdes.2010.12.019

Filiberto, J., Gross, J., & McCubbin, F. M. (2016). Constraints on the water, chlorine, and fluorine content of the Martian mantle. *Meteoritics & Planetary Sciences*, *51*(11), 2023–2035. https://doi.org/10.1111/maps.12624

Filiberto, J., & Treiman, A. H. (2009). Martian magmas contained abundant chlorine, but little water. *Geology*, *37*(12), 1087–1090. https://doi.org/10.1130/G30488A10.1130/g30488a.1

Fogel, R. A., & Rutherford, M. J. (1995). Magmatic volatiles in primitive lunar glasses: I. FTIR and EPMA analyses of Apollo 15 green and yellow glasses and revision of the volatile-assisted fire-fountain theory. *Geochimica et Cosmochimica Acta*, *59*, 201–215. https://doi.org/10.1016/0016-7037(94)00377-X

Gaddis, L. R., Hawke, B. R., Robinson, M. S., & Coombs, C. (2000). Compositional analyses of small lunar pyroclastic deposits using Clementine multispectral data. *Journal of Geophysical Research*, *105*, 4245–4262. https://doi.org/10.1029/1999JE001070

Gaddis, L. R., Pieters, C. M., & Hawke, B. R. (1985). Remote sensing of lunar pyroclastic mantling deposits. *Icarus*, *61*, 461–489. https://doi.org/10.1016/0019-1035(85)90136-8

Gaddis, L. R., Staid, M. I., Tyburczy, J. A., Hawke, B. R., & Petro, N. E. (2003). Compositional analyses of lunar pyroclastic deposits. *Icarus*, *161*(2), 262–280. https://doi.org/10.1016/S0019-1035(02)00036-2

Garry, W. B., Zimbelman, J. R., & Gregg, T. K. P. (2007). Morphology and emplacement of a long-channelled lava flow near Ascraeus Mons Volcano, Mars. *Journal of Geophysical Research*, *112*, 1–21. https://doi.org/10.1029/2006JE002803

Gerlach, T. M., McGee, K. A., Elias, T., Sutton, A. J., & Doukas, M. P. (2002). Carbon dioxide emission rate of Kilauea volcano: Implications for primary magma and the summit reservoir. *Journal of Geophysical Research*, *107*(B9), 2189. https://doi.org/10.1029/2001JB00040

Ghiorso, M. S., & Gualda, G. A. R. (2015). An H_2O–CO_2 mixed fluid saturation model compatible with rhyolite-MELTS. *Contributions to Mineralogy and Petrology*, *169*(53). https://doi.org/10.1007/s00410-015-1141-8

Giordano, D., & Dingwell, D. B. (2003). Viscosity of hydrous Etna basalt: Implications for Plinian-style basaltic eruptions. *Bulletin of Volcanology*, *65*, 8–14. https://doi.org/10.1007/s00445-002-0233-2

Giordano, D., Russell, J. K., & Dingwell, D. B. (2008). Viscosity of magmatic liquids: A model. *Earth and Planetary Science Letters*, *271*, 123–134. https://doi.org/10.1016/j.epsl.2008.03.038

Glaze, L. S., & Baloga, S. M. (2006). Rheologic inferences from the levees of lava flows on Mars. *Journal of Geophysical Research*, *111*(E09006), 1–10. https://doi.org/10.1029/2005JE002585

Goudge, T. A., Head, J. W., Kerber, L., Blewett, D. T., Denevi, B. W., Domingue, D. L., et al. (2014). Global inventory and characterization of pyroclastic deposits on Mercury: New insights into pyro-clastic activity from MESSENGER orbital data. *Journal of Geophysical Research*, *119*, 635–658. https://doi.org/10.1002/2013JE004480

Greenwood, J. P., Karato, S., Vander Kaaden, K. E., Pahlevan, K., & Usui, T. (2018). Water and volatile inventories of Mercury, Venus, the Moon, and Mars. *Space Science Reviews*, *214*(5). https://doi.org/10.1007/s11214-018-0526-1

Grove, T. L., & Krawczynski, M. J. (2009). Lunar mare volcanism: Where did the magmas come from? *Elements*, *5*(1), 29–34. https://doi.org/10.2113/gselements.5.1.29

Gualda, G. A. R., Ghiorso, M. S., Lemons, R. V., & Carley, T. L. (2012). Rhyolite-MELTS: A modified calibration of MELTS Optimized for silica-rich, fluid-bearing magmatic systems. *Journal of Petrology*, *53*, 875–890. https://doi.org/10.1093/petrology/egr080

Gustafson, J. O., Bell, J. F., Gaddis, L. R., Hawke, B. R., & Giguere, T. A. (2012). Characterization of previously unidentified lunar pyroclastic deposits using Lunar Reconnaissance Orbiter Camera data. *Journal of Geophysical Research*, *117*, 1–21. https://doi.org/10.1029/2011JE003893

Hartmann, W. K. (2014). The giant impact hypothesis: Past, present (and future?). *Philosophical Transactions of the Royal Society A*, *372*, 20130249. https://doi.org/10.1098/rsta.2013.0249

Hartmann, W. K., & Davis, D. R. (1974). Satellite-sized planetesimals and lunar origin. *Icarus*, *24*(4), 504–515. https://doi.org/10.1016/0019-1035(75)90070-6

Hauri, E. H., Weinreich, T., Saal, A. E., Rutherford, M. C., & Van Orman, J. A. (2011). High pre-eruptive water contents preserved in lunar melt inclusions. *Science*, *333*, 213–216. https://doi.org/10.1126/science.1204626

Hawke, B. R., Coombs, C., Gaddis, L. R., Lucey, P. G., & Owensby, P. D. (1989). Remote sensing and geologic studies of localized dark mantle deposits on the Moon. In *Proceedings of the lunar science conference* (pp. 255–268). Lunar and Planetary Institute.

Head, J. W., & Wilson, L. (1979). Alphonsus-type dark-halo craters: Morphology, morphometry and eruption conditions. In *Proceedings of the lunar and planetary science conference* (pp. 2861–2897). Lunar and Planetary Institute.

Head, J. W., & Wilson, L. (2017). Generation, ascent and eruption of magma on the Moon: New insights into source depths, magma supply, intrusions and effusive/explosive eruptions (Part 2: Predicted emplacement processes and observations). *Icarus*, *283*, 176–223. https://doi.org/10.1016/j.icarus.2015.12.03910.1016/j.icarus.2016.05.031

Head, J. W., Wilson, L., Deutsch, A. N., Rutherford, M. J., & Saal, A. J. (2020). Volcanically Induced Transient Atmospheres on the Moon: Assessment of Duration, Significance, and Contributions to Polar Volatile Traps. *Geophysical Research Letters*, *47*(18), e2020GL089509. https://doi.org/10.1029/2020GL089509

Heiken, G. H., McKay, D. S., & Brown, R. W. (1974). Lunar deposits of possible pyroclastic origin. *Geochimica et Cosmochimica Acta*, *38*, 1703–1704. https://doi.org/10.1016/0016-7037(74)90187-2

Hekinian, R., Pineau, F., Shilobreeva, S., Bideau, D., Gracia, E., & Javoy, M. (2000). Deep sea explosive activity on the Mid-Atlantic Ridge near 34°50′ N: Magma composition, vesicularity, and volatile content. *Journal of Volcanology and Geothermal Research*, *98*, 4. https://doi.org/10.1016/S0377-0273(99)00190-0

Hess, P. C. (2000). On the source region for mare picritic glasses. *Journal of Geophysical Research*, *105*(E2), 4347–4360. https://doi.org/10.1029/1999JE001067

Hiesinger, H., Head, J. W., Wolf, U., Jaumann, R., & Neukum, G. (2011). Ages and stratigraphy of lunar mare basalts: A synthesis. *GSA Special Papers*, *477*, 1–51. https://doi.org/10.1029/2009JE003380

Hirschmann, M. M., Withers, A. C., Ardia, P., & Foley, N. T. (2012). Solubility of molecular hydrogen in silicate melts and consequences for volatile evolution of terrestrial planets. *Earth and Planetary Science Letters*, *345*(348), 38–48. https://doi.org/10.1016/j.epsl.2012.06.031

Holloway, J. R., & Blank, J. G. (1994). Application of experimental results to C–O–H species in natural melts. In volatiles in magmas. *Reviews in Mineralogy*, *30*, 187–230. https://doi.org/10.1515/9781501509674-012

Horowitz, H. M., Jacob, D. J., Zhang, Y., Dibble, T. S., Slemr, F., Amos, H. M., et al. (2017). A new mechanism for atmospheric mercury redox chemistry: Implications for the global mercury budget. *Atmospheric Chemistry and Physics*, *17*, 6353–6371. https://doi.org/10.5194/acp-17-6353-2017

Hughes, S. S., Delano, J. W., & Schmitt, R. A. (1988). Apollo 15 yellow-brown volcanic glass: Chemistry and petrogenetic relations to green volcanic glass and olivine-normative mare basalts. *Geochimica et Cosmochimica Acta*, *52*, 2379–2391. https://doi.org/10.1016/0016-7037(88)90295-5

Hulme, G. (1976). The determination of the rheological properties and effusion rate of an Olympus Mons lava. *Icarus*, *27*(2), 207–213. https://doi.org/10.1016/0019-1035(76)90004-X

Iman, R. L., & Conover, W. J. (1980). Small sample sensitivity analysis techniques for computer models with an application to risk assessment. *Communications in Statistics - Theory and Methods*, *9*(17), 1–95. https://doi.org/10.1080/03610928008827996

Jolliff, B. L., Wieczorek, M. A., Shearer, C. K., & Neal, C. R. (2006). *New views of the Moon*. De Gruyter.

Jones, T. J., Reynolds, C. D., & Boothroyd, S. C. (2019). Fluid dynamic induced break-up during volcanic eruptions. *Nature Communications*, *10*, 3828. https://doi.org/10.1038/s41467-019-11750-4

Kavanagh, J. L., & Sparks, R. S. J. (2011). Insights of dyke emplacement mechanics from detailed 3D dyke thickness datasets. *Journal of the Geological Society*, *168*, 965–978. https://doi.org/10.1144/0016-76492010-137

Kerber, L., Head, J. W., Blewett, D. T., Solomon, S. C., Wilson, L., Murchie, S. L., et al. (2011). The global distribution of pyroclastic deposits on Mercury: The view from MESSENGER flybys 1–3. *Planetary and Space Science*, *59*, 1895–1909. https://doi.org/10.1016/j.pss.2011.03.020

Kerber, L., Head, J. W., Solomon, S., Murchie, S., Blewett, D., & Wilson, L. (2009). Explosive volcanic eruptions on Mercury: Eruption conditions, magma volatile content, and implications for interior volatile abundances. *Earth and Planetary Science Letters*, *285*(3–4), 263–271. https://doi.org/10.1016/j.epsl.2009.04.037

Kerber, L., Head, J. W., Solomon, S. C., Murchie, S. L., Blewett, D. T., & Wilson, L. (2009). Explosive volcanic eruptions on Mercury: Eruption conditions, magma volatile content, and implications for mantle volatile abundances. *Earth and Planetary Science Letters*, *285*, 263e271. https://doi.org/10.1016/j.epsl.2009.04.037

Klausen, M. B. (2006). Similar dyke thickness variation across three volcanic rifts in the North Atlantic region: Implications for intrusion mechanisms. *Lithos*, *92*(1–2), 137–152. https://doi.org/10.1016/j.lithos.2006.03.030

La Spina, G., Arzilli, F., Llewellin, E. W., Burton, M. R., Clarke, A. B., de' Michieli Vitturi, M., et al. (2021). Explosivity of basaltic lava fountains is controlled by magma rheology, ascent rate and outgassing. *Earth and Planetary Science Letters*, *553*, 1–11. https://doi.org/10.1016/j.epsl.2020.116658

La Spina, G., Burton, M. R., & de' Michieli Vitturi, M. (2015). Temperature evolution during magma ascent in basaltic effusive eruptions: A numerical application to Stromboli volcano. *Earth and Planetary Science Letters*, *426*, 89–100. https://doi.org/10.1016/j.epsl.2015.06.015

La Spina, G., Burton, M. R., de' Michieli Vitturi, M., & Arzilli, F. (2016). Role of syn-eruptive plagioclase disequilibrium crystallization in basaltic magma ascent dynamics. *Nature Communications*, *7*, 13402. https://doi.org/10.1038/ncomms13402

La Spina, G., Clarke, A. B., de' Michieli Vitturi, M., Burton, M. R., Allison, C. M., Roggensack, K., & Alfano, F. (2019). Conduit dynamics of highly explosive basaltic eruptions: The 1085 CE Sunset Crater sub-Plinian events. *Journal of Volcanology and Geothermal Research*, *387*, 106658. https://doi.org/10.1016/j.jvolgeores.2019.08.001

La Spina, G., & de' Michieli Vitturi, M. (2012). High-resolution finite volume central schemes for a compressible two-phase model. *SIAM Journal on Scientific Computing*, *34*, B861–B880. https://doi.org/10.1137/12087089x

La Spina, G., de' Michieli Vitturi, M., & Romenski, E. (2014). A compressible single-temperature conservative two-phase model with phase transitions. *International Journal for Numerical Methods in Fluids*, *76*, 282–311. https://doi.org/10.1002/fld.3934

La Spina, G., Polacci, M., Burton, M. R., & de' Michieli Vitturi, M. (2017). Numerical investigation of permeability models for low viscosity magmas: Application to the 2007 Stromboli effusive eruption. *Earth and Planetary Science Letters*, *473*, 279–290. https://doi.org/10.1016/j.epsl.2017.06.013

Lanz, J. K., Wagner, R., Wolf, U., Kröchert, J., & Neukum, G. (2010). Rift zone volcanism and associated cinder cone field in Utopia Planitia, Mars. *Journal of Geophysical Research*, *115*(E12019), 1–21. https://doi.org/10.1029/2010JE003578

Le Bas, M. J. (2000). IUGS reclassification of the high-Mg and picritic volcanic rocks. *Journal of Petrology*, *41*(10), 1467–1470. https://doi.org/10.1093/petrology/41.10.1467

Lena, R., Wöhler, C., Bregante, M. T., Lazzarotti, P., & Lammel, S. (2008). Lunar domes in Mare Undarum: Spectral and morphometric properties, eruption conditions, and mode of emplacement. *Planetary and Space Science*, *56*(3–4), 553–569. https://doi.org/10.1016/j.pss.2007.11.010

Leshin, L. A., Epstein, S., & Stolper, E. M. (1996). Hydrogen isotope geochemistry of SNC meteorites. *Geochimica et Cosmochimica Acta*, *60*, 2635–2650. https://doi.org/10.1016/0016-7037(96)00122-6

Lister, J. R., & Kerr, R. C. (1991). Fluid-mechanical models of crack propagation and their application to magma transport in dykes. *Journal of Geophysical Research*, *96*(B6), 10049–10077. https://doi.org/10.1029/91JB00600

Llewellin, E. W., Mader, H. M., & Wilson, S. D. R. (2002). The constitutive equation and flow dynamics of bubbly magmas. *Geophysical Research Letters*, *29*, 2170. https://doi.org/10.1029/2002GL015697

Lo, M., La Spina, G., Joy, K., Polacci, M., Burton, M. (2021). *Determining the effect of varying magmatic volatile content on lunar magma ascent dynamics*. University of Manchester Collection. https://doi.org/10.48420/c.5557635.v1

Mader, H. M., Llewellin, E. W., & Mueller, S. P. (2013). The rheology of two-phase magmas: A review and analysis. *Journal of Volcanology and Geothermal Research*, *257*, 135–158. https://doi.org/10.1016/j.jvolgeores.2013.02.014

McCubbin, F. M., Hauri, E. H., Elardo, S. M., Vander Kaaden, K. E., Wang, J., & Shearer, C. K. (2012). Hydrous melting of the Martian mantle produced both depleted and enriched shergottites. *Geology*, *40*, 683–686. https://doi.org/10.1130/G33242.1

McCubbin, F. M., Vander Kaaden, K. E., Tartèse, R., Klima, R. L., Liu, Y., Mortimer, J., et al. (2015). Magmatic volatiles (H, C, N, F, S, Cl) in the lunar mantle, crust, and regolith: Abundances, distributions, processes, and reservoirs. *American Mineralogist*, *100*, 1668–1707. https://doi.org/10.2138/am-2015-4934CCBYNCND

McKay, M. D., Beckman, R. J., & Conover, W. J. (1979). A comparison of three methods for selecting values of input variables in the analysis of output from a computer code. *Technometrics*, *42*(1), 55–61. https://doi.org/10.1080/00401706.1979.10489755

McSween, H. Y., Grove, T. L., Lentz, R. C., Dann, J. C., Holzheid, A. H., Riciputi, L. R., & Ryan, J. G. (2001). Geochemical evidence for magmatic water within Mars from pyroxenes in the Shergotty meteorite. *Nature*, *409*, 487–490. https://doi.org/10.1038/35054011

Melnik, O., & Sparks, R. S. J. (2002). *Dynamics of magma ascent and lava extrusion at Soufrière Hills Volcano, Montserrat* (pp. 153–171). London, Memoirs: Geological Society. https://doi.org/10.1144/GSL.MEM.2002.021.01.07

Moore, G., Vennemann, T., & Carmichael, I. S. E. (1995). Solubility of water in magmas to 2 kbar. *Geology*, *23*(12), 1099–1102. https://doi.org/10.1130/0091-7613(1995)023%3C1099:SOWIMT%3E2.3.CO;2

Moore, G., Vennemann, T., & Carmichael, I. S. E. (1998). An empirical model for the solubility of H_2O in magmas to 3 kilobars. *American Mineralogist*, *83*(1–2), 36–42. https://doi.org/10.2138/am-1998-1-203

Moore, H. J., Arthur, W., & Schaber, G. G. (1978). Yield strengths of flows on Earth, Mars, and Moon. In *Proceedings of the lunar and planetary science conference* (pp. 3351–3378). Lunar and Planetary Institute.

Morgan, C., Wilson, L., & Head, J. W. (2021). Formation and dispersal of pyroclasts on the Moon: Indicators of lunar magma volatile contents. *Journal of Volcanology and Geothermal Research*, *413*, 107217. https://doi.org/10.1016/j.jvolgeores.2021.107217

Moune, S., Faure, F., Gauthier, P.-J., & Sims, K. W. W. (2007). Pele's hairs and tears: Natural probe of volcanic plume. *Journal of Volcanology and Geothermal Research*, *164*, 244–253. https://doi.org/10.1016/j.jvolgeores.2007.05.007

Mysen, B. O., & Wheeler, K. (2000). Solubility behavior of water in haploandesitic melts at high pressure and high temperature. *American Mineralogist*, *85*(9), 1128–1142. https://doi.org/10.2138/am-2000-8-903

Namiki, A., & Manga, M. (2008). Transition between fragmentation and permeable outgassing of low viscosity magmas. *Journal of Volcanology and Geothermal Research*, *169*, 48–60. https://doi.org/10.1016/j.jvolgeores.2007.07.020

Neal, C. R., & Taylor, L. A. (1992). Petrogenesis of mare basalts: A record of lunar volcanism. *Geochimica et Cosmochimica Acta*, *56*(6), 2177–2211. https://doi.org/10.1016/0016-7037(92)90184-K

Needham, D. H., & Kring, D. A. (2017). Lunar volcanism produced a transient atmosphere around the ancient Moon. *Earth and Planetary Science Letters*, *478*, 175–178. https://doi.org/10.1016/j.epsl.2017.09.002

Nekvasil, H., Filiberto, J., McCubbin, F. M., & Lindsley, D. H. (2007). Alkalic parental magmas for the chassignites? *Meteoritics & Planetary Sciences*, *42*, 979–992. https://doi.org/10.1111/j.1945-5100.2007.tb01145.x

Nicholis, M. G., & Rutherford, M. J. (2009). Graphite oxidation in the Apollo 17 orange glass magma: Implications for the generation of a lunar volcanic gas phase. *Geochimica et Cosmochimica Acta*, *73*, 5905–5917. https://doi.org/10.1016/j.gca.2009.06.022

Papale, P. (1999). Strain-induced magma fragmentation in explosive eruptions. *Nature*, *397*, 425–428. https://doi.org/10.1038/17109

Papale, P. (2001). Dynamics of magma flow in volcanic conduits with variable fragmentation efficiency and nonequilibrium pumice degassing. *Journal of Geophysical Research*, *106*(B6), 11043–11065. https://doi.org/10.1029/2000JB900428

Papale, P., & Dobran, F. (1994). Magma flow along the volcanic conduit during the Plinian and pyroclastic flow phases of the May 18, 1980, Mount St. Helens eruption. *Journal of Geophysical Research*, *99*(B3), 4355–4373. https://doi.org/10.1029/93JB02972

Qian, Y., Xiao, L., Head, J. W., van der Bogert, C. H., Hiesinger, H., & Wilson, L. (2021). Young lunar mare basalts in the Chang'e-5 sample return region, northern Oceanus Procellarum. *Earth and Planetary Science Letters*, *555*, 116702. https://doi.org/10.1016/j.epsl.2020.116702

Renggli, C. J., King, P. L., Henley, R. W., & Norman, M. D. (2017). Volcanic gas composition, metal dispersion and deposition during explosive volcanic eruptions on the Moon. *Geochimica et Cosmochimica Acta*, *206*, 296–311. https://doi.org/10.1016/j.gca.2017.03.012

Romenski, E., Drikakis, D., & Toro, E. (2010). Conservative models and numerical methods for compressible two-phase flow. *Journal of Scientific Computing*, *42*, 68–95. https://doi.org/10.1007/s10915-009-9316-y

Rutherford, M. J., Head, J. W., Saal, A. E., Hauri, E. H., & Wilson, L. (2017). Model for the origin, ascent, and eruption of lunar picritic magmas. *American Mineralogist*, *102*(10), 2045–2053. https://doi.org/10.2138/am-2017-5994ccbyncnd

Rutherford, M. J., & Papale, P. (2009). Origin of basalt fire-fountain eruptions on Earth versus the Moon. *Geology*, *37*(3), 219–222. https://doi.org/10.1130/G25402A.1

Saal, A. E., Hauri, E. H., Lo Cascio, M., Van Orman, J. A., Rutherford, M. C., & Cooper, R. F. (2008). Volatile content of lunar volcanic glasses and the presence of water in the Moon's interior. *Nature*, *454*, 192–196. https://doi.org/10.1038/nature07047

Sato, M. (1979). The driving mechanism of lunar pyroclastic eruptions inferred from the oxygen fugacity behaviour of Apollo 17 orange glass. In *Proceedings of the lunar and planetary science conference* (pp. 311–325). Lunar and Planetary Institute

Sharp, Z. D., McCubbin, F. M., & Shearer, C. M. (2011). A unifying theory for lunar water. *Paper presented at American Geophysical Union Fall Meeting*. San Francisco, California, United States.

Shearer, C. K., Hess, P. C., Wieczorek, M. A., Pritchard, M. E., Parmentier, E. M., Borg, L. E., et al. (2006). Thermal and magmatic evolution of the Moon. *Reviews in Mineralogy and Geochemistry*, *60*(1), 365–518. https://doi.org/10.2138/rmg.2006.60.4

Shearer, C. K., & Papike, J. J. (1993). Basaltic magmatism on the Moon: A perspective from volcanic picritic glass beads. *Geochimica et Cosmochimica Acta*, *57*, 4785–4812. https://doi.org/10.1016/0016-7037(93)90200-G

Shearer, C. K., & Papike, J. J. (2004). Oxygen fugacity of lunar basalts and the lunar mantle. Range of fO_2 and the effectiveness of oxybarometers. In *Workshop on oxygen in the terrestrial Planets, #3025. LPI contribution No. 1203*. Lunar and Planetary Institute

Shearer, C. K., Papike, J. J., Simon, S. B., Shimizu, N., Yurimoto, Y., & Sueno, S. (1990). Ion microprobe studies of trace elements in Apollo 14 volcanic glass beads: Comparisons to Apollo 14 mare basalts and petrogenesis of picritic magmas. *Geochimica et Cosmochimica Acta*, *54*, 851–867. https://doi.org/10.1016/0016-7037(90)90378-X

Sigurdsson, H. (2015). *The encyclopedia of volcanoes*. Elsevier.

Sparks, R. S. J. (1978). The dynamics of bubble formation and growth in magmas: A review and analysis. *Journal of Volcanology and Geothermal Research*, *3*(1–2), 1–37. https://doi.org/10.1016/0377-0273(78)90002-1

Spera, F. J. (1992). Lunar magma transport phenomena. *Geochimica et Cosmochimica Acta*, *56*(6), 2253–2265. https://doi.org/10.1016/0016-7037(92)90187-N

Spudis, P. D. (2015). Volcanism on the Moon. In H. Sigurdsson (Ed.), *The encyclopedia of volcanoes* (pp. 689–700). Elsevier. https://doi.org/10.1016/b978-0-12-385938-9.00039-0

Steele, A., McCubbin, F. M., Fries, M., Glamoclija, M., Kater, L., & Nekvasil, H. (2010). Graphite in an Apollo 17 impact melt breccia. *Science*, *329*, 51. https://doi.org/10.1126/science.1190541

Tartèse, R., Anand, M., Barnes, J. J., Starkey, N. A., Franchi, I. A., & Sano, Y. (2013). The abundance, distribution, and isotopic composition of Hydrogen in the Moon as revealed by basaltic lunar samples: Implications for the volatile inventory of the Moon. *Geochimica et Cosmochimica Acta*, *122*, 58–74. https://doi.org/10.1016/j.gca.2013.08.014

Taylor, G. J., Warren, P., Ryder, G., Delano, J., Pieters, C., & Lofgren, G. (1991). Lunar rocks. In G. H. Heiken, D. T. Vaniman, & B. M. French (Eds.), *Lunar sourcebook* (pp. 183–284). Cambridge University Press.

Thomas, R. J., Rothery, D. A., Conway, S. J., & Anand, M. (2014). Long-lived explosive volcanism on Mercury. *Geophysical Research Letters*, *41*, 6084–6092. https://doi.org/10.1002/2014GL061224

Thomas-Keprta, K. L., Clemett, S. J., Messenger, S., Ross, D. K., Le, L., Rahman, Z., et al. (2014). Organic matter on the Earth's Moon. *Geochimica et Cosmochimica Acta*, *134*, 1–15. https://doi.org/10.1016/j.gca.2014.02.047

Trang, D., Gillis-Davis, J. J., Lemelin, M., Cahill, J. T. S., Hawke, B. R., & Giguere, T. A. (2017). The compositional and physical properties of localized lunar pyroclastic deposits. *Icarus*, *283*, 232–253. https://doi.org/10.1016/j.icarus.2016.09.025

Wang, Y., Guan, Y., Hsu, W., & Eiler, J. M. (2012). Water content, chlorine and hydrogen isotope compositions of lunar apatite. *Paper presented at 75th Annual Meteoritical Society Meeting*. Cairns, Australia.

Webb, S. L., & Dingwell, D. B. (1990). The onset of non-Newtonian rheology of silicate melts. *Physics and Chemistry of Minerals*, *17*, 125–132. https://doi.org/10.1007/BF00199663

Weitz, C. M., Head, J. W., & Pieters, C. M. (1998). Lunar regional dark mantle deposits: Geologic, multispectral, and modelling studies. *Journal of Geophysical Research*, *103*(E10), 22725–22759. https://doi.org/10.1029/98JE02027

Wetzel, D. T., Hauri, E. H., Saal, A. E., & Rutherford, M. J. (2015). Carbon content and degassing history of the lunar volcanic glasses. *Nature Geoscience*, *8*(10), 755–758. https://doi.org/10.1038/ngeo2511

Wetzel, D. T., Rutherford, M. J., Jacobsen, S. D., Hauri, E. H., & Saal, A. E. (2013). Degassing of reduced carbon from planetary basalts. *Proceedings of the National Academy of Sciences*, *110*(20), 8010–8013. https://doi.org/10.1073/pnas.1219266110

Wieczorek, M. A., Neumann, G. A., Nimmo, F., Kiefer, W. S., Taylor, G. J., Melosh, H. J., et al. (2013). The Crust of the Moon as seen by GRAIL. *Science*, *339*(6120), 671–675. https://doi.org/10.1126/science.1231530

Williams, D. A., Fagents, S. A., & Greeley, R. (2000). A reassessment of the emplacement and erosional potential of turbulent, low-viscosity lavas on the Moon. *Journal of Geophysical Research*, *105*(E8), 20189–20205. https://doi.org/10.1029/1999JE001220

Wilson, L. (1972). Explosive volcanic eruptions – II The atmospheric trajectories of pyroclasts. *Geophysical Journal of the Royal Astronomical Society*, *30*, 381–392. https://doi.org/10.1111/j.1365-246X.1972.tb05822.x

Wilson, L. (1980). Relationships between pressure, volatile content and ejecta velocity in three types of volcanic explosion. *Journal of Volcanology and Geothermal Research*, *8*(2–4), 297–313. https://doi.org/10.1016/0377-0273(80)90110-9

Wilson, L., & Head, J. W. (1981). Ascent and eruption of basaltic magma on the Earth and Moon. *Journal of Geophysical Research*, *86*(NB4), 2971–3001. https://doi.org/10.1029/JB086iB04p02971

Wilson, L., & Head, J. W. (2003). Deep generation of magmatic gas on the Moon and implication for pyroclastic eruptions. *Geophysical Research Letters*, *30*(12), 1605–1609. https://doi.org/10.1029/2002GL016082

Wilson, L., & Head, J. W. (2017). Generation, ascent and eruption of magma on the Moon: New insights into source depths, magma supply, intrusions and effusive/explosive eruptions (Part 1: Theory). *Icarus*, *283*, 146–175. https://doi.org/10.1016/j.icarus.2015.12.039

Wilson, L., & Head, J. W. (2018). Controls on lunar basaltic volcanic eruption structure and morphology: Gas release patterns in sequential eruption phases. *Geophysical Research Letters*, *45*(12), 5852–5859. https://doi.org/10.1029/2018GL078327

Wilson, L., Mouginis-Mark, P. J., Tyson, S., Mackown, J., & Garbeil, H. (2009). Fissure eruptions in Tharsis, Mars: Implications for eruption conditions and magma sources. *Journal of Volcanology and Geothermal Research*, *185*(1–2), 28–46. https://doi.org/10.1016/j.jvolgeores.2009.03.006

Yoshida, S., & Koyaguchi, T. (1999). A new regime of volcanic eruption due to the relative motion between liquid and gas. *Journal of Volcanology and Geothermal Research*, *89*(1–4), 303–315. https://doi.org/10.1016/S0377-0273(99)00005-0

Zolotov, M. Y. (2010). On the chemistry of mantle and magmatic volatiles on Mercury. *Icarus*, *212*(1), 24–41. https://doi.org/10.1016/j.icarus.2010.12.014